Identifying climate model structural inconsistencies allows for tight constraint of aerosol radiative forcing

Leighton A. Regayre[1,2], Lucia Deaconu[3,4], Daniel P. Grosvenor[1,2,5], David M. H. Sexton[2], Christopher Symonds[5], Tom Langton[3], Duncan Watson-Paris[3], Jane P. Mulcahy[2], Kirsty J. Pringle[1,5,6], Mark Richardson[5], Jill S. Johnson[1,7], John W. Rostron[2], Hamish Gordon[1,8], Grenville Lister[9,10], Philip Stier[3] and Ken S. Carslaw[1]

[1]Institute for Climate and Atmospheric Science, School of Earth and Environment, University of Leeds, Leeds, LS2 9JT, UK
[2]Met Office Hadley Centre, Exeter, Fitzroy Road, Exeter, Devon, EX1 3PB, UK
[3]Atmospheric, Oceanic and Planetary Physics Department, University of Oxford, Oxford, OX1 3PU
[4]Faculty of Environmental Science and Engineering, Babes-Bolyai University, Cluj, Romania, 400294
[5]Centre for Environmental Modelling and Computation, School of Earth and Environment, University of Leeds, Leeds, LS2 9JT, UK
[6]Edinburgh Parallel Computing Centre, Bayes Centre, University of Edinburgh, EH8 9BT
[7]School of Mathematics and Statistics, University of Sheffield, Sheffield, S3 7RH, UK
[8]Department of Chemical Engineering and Center for Atmospheric Particle Studies, Carnegie Mellon University, Pittsburgh, PA 15213,USA
[9]Department of Meteorology, University of Reading, RG6 6AH, UK
[10]National Centre for Atmospheric Science, Reading, RG6 6AH, UK

Correspondence to: Leighton A. Regayre (L.A.Regayre@leeds.ac.uk)

Abstract. Aerosol radiative forcing uncertainty affects estimates of climate sensitivity and limits model skill at making climate projections. Efforts to improve the representations of physical processes in climate models, including extensive comparisons with observations, have not significantly constrained the range of possible aerosol forcing values. A far stronger constraint, in particular for the lower (most-negative) bound, can be achieved using global mean energy-balance arguments based on observed changes in historical temperature. Here, we show that structural deficiencies in a climate model, revealed as inconsistencies among observationally constrained cloud properties in the model, limit the effectiveness of observational constraint of the uncertain physical processes. We sample uncertainty in 37 model parameters related to aerosols, clouds and radiation in a perturbed parameter ensemble of the UK Earth System Model and evaluate 1 million model variants (different parameter settings from Gaussian Process emulators) against satellite-derived observations over several cloudy regions. We show that it is possible to reduce the parametric uncertainty in global mean aerosol forcing by more than 50%, constraining it to a range in close agreement with energy-balance constraints (around -1.3 to -0.1 W m^{-2}). However, our analysis of a very large set of model variants exposes model internal inconsistencies that would not be apparent in a small set of model simulations. Incorporating observations associated with these inconsistencies weakens the forcing constraint because they require a wider range of parameter values to accommodate conflicting information. Our estimated aerosol forcing range is the maximum feasible constraint using our structurally imperfect model and the chosen observations. Structural model developments targeted at the identified inconsistencies would enable a larger set of observations to be used for constraint,

which would then narrow the uncertainty further. Such an approach provides a rigorous pathway to improved model realism and reduced uncertainty that has so far not been achieved through the normal model development approach.

1 Introduction

The most uncertain component of human forcing of the climate system over the industrial period is aerosol effective radiative forcing (ΔF_{aer}; Forster et al., 2021). Uncertainty in historical ΔF_{aer} reduces our ability to confidently project near-term future changes to our climate (Andreae et al., 2005; Seinfeld et al., 2016; Peace et al., 2020; Fyfe et al., 2021). The best estimate of ΔF_{aer} based on current understanding of aerosols, clouds, radiation and their interactions (informed by results from global climate models and analysis of observations) ranges from -3.2 to -0.4 W m^{-2} (Bellouin et al., 2020). The magnitude of ΔF_{aer} has remained uncertain through all Intergovernmental Panel on Climate Change assessment reports (Forster et al., 2021), despite decades of research to improve our scientific understanding of the key processes and abundant observations with which to test models.

The lower (most-negative) bound on ΔF_{aer} is more tightly constrained by global mean energy balance arguments, which infer the magnitude indirectly based on historical emissions and changes in global mean surface temperature. Such studies suggest the lower bound may be around -1.8 to -1.7 W m^{-2} (e.g. Aldrin et al., 2012; Skeie et al., 2014, 2018). Evidence for a weaker (less negative) lower bound on ΔF_{aer} comes from energy-balance relationships that are additionally informed by output from global climate model ensembles. For example, Smith et al., (2021) constrain the ΔF_{aer} lower bound to around -1.5 W m^{-2} and Albright et al., (2021) constrain the lower bound to between -1.8 and -1.3 W m^{-2}. However, tight constraint of just the magnitude of historical and future global mean ΔF_{aer} does not produce a climate model that can be used to explore the full range of regional and global climatic effects. Thus, although energy-balance constraints and emergent constraint methods (e.g. Watson-Parris et al., 2020) can set the plausible bounds on historical global mean ΔF_{aer} (and/or its components), we also need a "process-based" approach of building reliable global climate models that can accurately simulate the observed state and behaviour of aerosols, clouds and radiation that will determine the regional patterns of aerosol effects on future climate (Williams et al., 2022).

A process-based constraint of ΔF_{aer} is a substantial undertaking, with many steps involved. It relies mainly on using complex climate models to simulate the underlying physical processes that affect changes in aerosols, clouds and radiation (and hence ΔF_{aer}), then settling on models that have been developed and refined to achieve acceptable agreement with extensive observations of these atmospheric properties and trends. It is assumed that good agreement of a model with observations ensures that the model is able to make trustworthy estimates of ΔF_{aer}, which cannot itself be observed. Yet, the process-based uncertainty range has remained far wider than estimates from energy balance approaches because models simulate a very large number of complex and regionally varying processes that can affect the magnitude of global mean ΔF_{aer} (Carslaw et al., 2013; Regayre et al., 2015; Qian et al., 2018; Yoshioka et al., 2019).

A further challenge in process-based constraint is that the range of ΔF_{aer} stems from two sources of uncertainty in climate models: structural uncertainty and parametric uncertainty. Structural deficiencies in a model are associated with coding choices related to spatial resolution, numerical methods, parametrisation schemes, and neglected processes. Model
70   developments attempt to reduce these deficiencies and the biases they cause compared to observations, and multi-model intercomparisons (Gliß et al., 2021; Thornhill et al., 2021) can be used to estimate a range of ΔF_{aer} across sets of structurally different models (structural uncertainty). Within a particular model, the uncertain parameters in the process equations cause an additional uncertainty in simulations of ΔF_{aer} (parametric uncertainty). Adjustment of parameter values, or tuning, is performed during and/or following model development to further improve the goodness-of-fit to observations (e.g. Hourdin et
75   al., 2017), although it is recognised that well-tuned models still have a large (and usually unquantified) parametric uncertainty (Lee et al., 2016). Perturbed parameter ensembles (PPEs) of the kind we use here (see Sect. 2.1.2) are a substantial extension of normal model tuning that explore many combinations of parameter values across their likely uncertainty ranges and quantify their combined effects on ΔF_{aer} (Carslaw et al., 2013; Regayre et al., 2018; Yoshioka et al., 2019). The resulting unconstrained parametric uncertainty in ΔF_{aer}, from sampling all important sources of uncertainty in our model, is larger than the range based
80   on energy balance constraints and approximately as wide as the multi-model range, suggesting that parametric uncertainties in ΔF_{aer} are as important as structural model differences.

Separation of structural and parametric sources of model uncertainty is important because they have different remedies. Structural uncertainties point to model deficiencies that require model developments, while parametric uncertainties can be reduced by matching the outputs of many model variants (parameter combinations) to historical observations through a process
85   called 'history matching' (Craig et al., 1997a; Williamson et al., 2013; Vernon et al., 2014; Johnson et al., 2020; Regayre et al., 2020). There is currently no best practice for accounting for and separating the effects of structural and parametric uncertainties (Sexton et al., 2012; Brynjarsdóttir and O'Hagan, 2014; McNeall et al., 2016; Johnson et al., 2020; Rostron et al., 2020). In particular, the observational constraint of parametric uncertainty cannot be cleanly separated from the effects of structural uncertainties. This is because, without accounting for potential (usually unquantified) structural errors, it may not be
90   possible to find any parameter combinations that produce a model that is consistent with all target observations. Therefore, it is common to add a structural error term during model-observation comparison (e.g. Sexton et al., 2012), which effectively inflates the parametric uncertainty and the overall model uncertainty to accommodate the structural errors. This approach avoids overfitting and provides an estimate of the uncertainty in ΔF_{aer} that broadly accounts for both sources of uncertainty. However, it does not provide any information about which processes cause structural model errors, nor how they weaken the
95   constraint of parameter values and the range of ΔF_{aer}.

To maximise ΔF_{aer} constraint, we need to address three key challenges. First, we need to densely sample the model parametric uncertainty related to the multitude of cloud, aerosol and physical atmosphere processes that determine ΔF_{aer}. Secondly, we need to identify model variables that share causes of uncertainty with ΔF_{aer}, to prioritise associated observations for use in the constraint process (Carslaw et al., 2013; Regayre et al., 2020). The final challenge is to ensure any constraint on
100 ΔF_{aer} is consistent across multiple observation types and/or quantify the limiting effect of any internal model inconsistencies

on ΔF_{aer} constraint. Here, we tackle these challenges using 1 million variants of the UKESM1-A model (based on statistical emulators trained on output from 221 model simulations) that sample ΔF_{aer} uncertainty (Sect. 3.1) caused by 37 aerosol, cloud and physical atmosphere model parameters (SI table S1). We evaluate the causes of uncertainty in cloud properties over stratocumulus-dominated regions (Sect. 3.2) and observationally constrain ΔF_{aer} using tens of thousands of combinations of more than 450 satellite-derived values (Sect.3.3). This approach exposes previously hidden structural inconsistencies related to representations of cloud properties in the model. We remove variables associated with these inconsistencies from the constraint process to produce an internally consistent constraint on ΔF_{aer}. This constraint does not make use of all available observations, therefore our central estimate of forcing may not be the final best value. However, we argue that in a model with fewer structural inconsistencies, our approach could constrain ΔF_{aer}, and associated process uncertainties even further.

2 Methods

Our approach is summarised in Fig. 1.
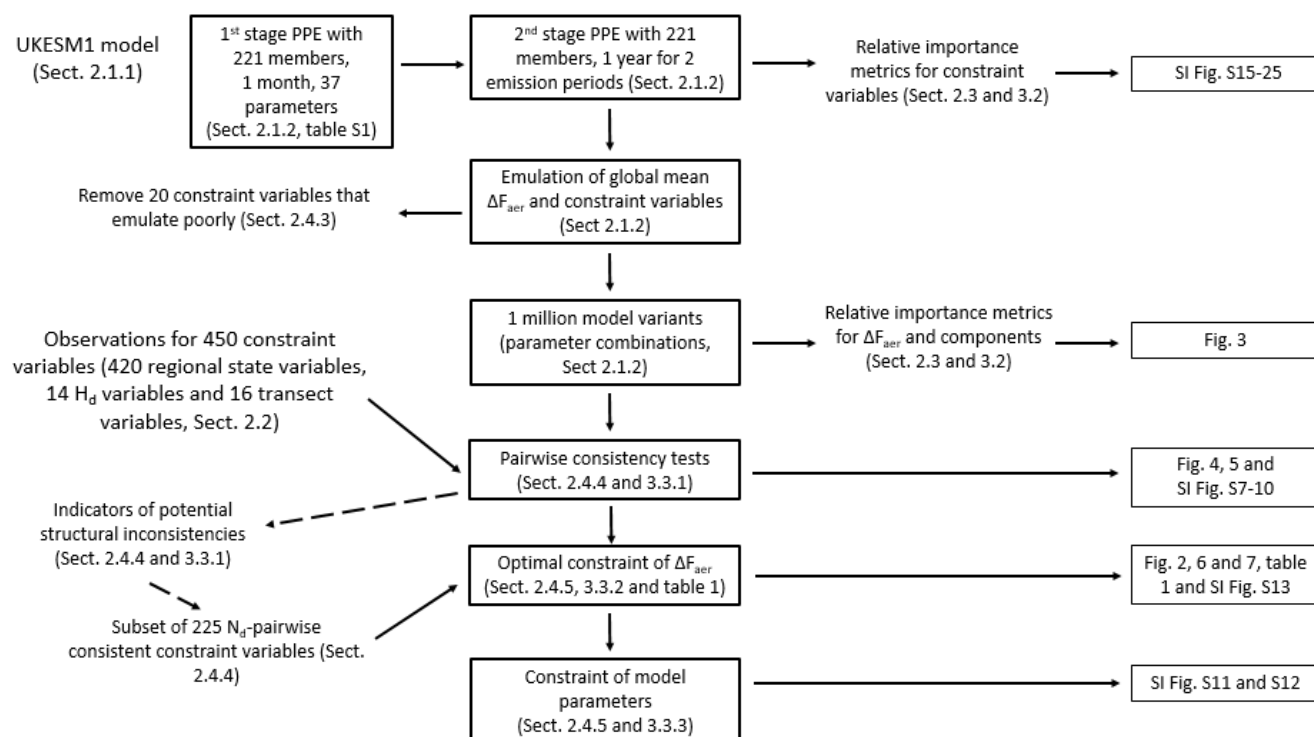
Figure 1: Flowchart detailing the procedure to densely sample model parameter uncertainty, evaluate model variants against observations, identify potential structural inconsistencies, and constrain ΔF_{aer}.

2.1 Experimental design

2.1.1 Model version

We used the atmosphere-only configuration of version 1 of the UK Earth System Model (UKESM1; Sellar et al., 2019) to create our PPEs (Sect. 2.1.2). UKESM1 was the model version submitted to the 6th Coupled Model Intercomparison Project

120 (CMIP6; Eyring et al., 2016). UKESM1 is based on the HADGEM3-GC3.1 physical climate model (Williams et al., 2018) with additional coupling to key Earth System processes (Sellar et al., 2019), including the United Kingdom Chemistry and Aerosol (UKCA) model (Archibald et al., 2019). The atmosphere-only configuration used here consists of the GA7.1 atmosphere (Walters et al., 2019; Mulcahy et al., 2020), with additional aerosol, cloud and physical atmosphere structural updates as implemented in UKESM1 (Mulcahy et al., 2020). GA7.1 includes several structural advancements to the aerosol

125 component of the model which significantly affect anthropogenic aerosol radiative forcing (Mulcahy et al., 2018). We refer to this model version as UKESM1-A.

We use an N96 horizontal resolution, which is $1.875 \times 1.25°$ (208 ×139 km) at the equator, with 85 vertical levels between the surface and 85km in altitude. Model vertical levels use a stretched grid such that the vertical resolution is around 13 m near the surface and around 150 to 200 m at the top of the boundary layer. We chose this resolution since it is the same

130 as that used for long climate runs in CMIP6.

Horizontal wind fields above around 2 km in our simulations (model vertical level 17) were nudged towards ERA-Interim values for the period December 2016 to November 2017. Nudging is intended to remove the effects of differences in large-scale meteorology between our PPE members, meaning we can attribute differences between model variants to perturbed parameter values. We do not nudge winds within the boundary layer, as many of our parameters are intended to affect

135 meteorological conditions, in particular cloud adjustments, in this part of the atmosphere.

The model was forced using anthropogenic SO_2 emissions, for the years 2014 and 1850, as prescribed in CMIP6 simulations. We calculated ΔF_{aer} as the difference in top-of-the-atmosphere radiative fluxes between these two periods. We accounted for above-cloud aerosol in our calculation of the components of ΔF_{aer} (Ghan et al., 2016) and aerosol-cloud interactions (Grosvenor and Carslaw, 2020).

140 Carbonaceous aerosol from fossil fuel and residential sources match those used in CMIP6 in our early-industrial simulations. However, in our present-day simulations we prescribed carbonaceous aerosol from biomass burning sources using emissions generated using Copernicus Atmospheric Monitoring Service Information for December 2016 to November 2017 (CAMS global biomass burning emissions based on fire radiative power; GFAS: data documentation) and spread these emissions between the surface and around 3km. We used emissions for the same period as prescribed wind fields, for the

145 closest possible comparison to observed values. In our early-industrial simulations (1850 anthropogenic SO_2 emissions) we similarly spread CMIP6 carbonaceous aerosol from biomass burning over model levels between the surface and around 3km.

We also prescribed, rather than simulated, sea surface temperatures and sea ice fraction to best match the December 2016 to November 2017 period. We prescribed land surface quantities, ocean surface concentrations of dimethylsulfide (DMS)

and chlorophyll, and atmospheric concentrations of gas species (including oxidants OH and O_3, which we then perturb), using
150   monthly mean output values from a fully-coupled version of the UKESM model, averaged over the 1979 to 2014 period.
Additionally, we prescribe volcanic SO_2 emissions for continuously emitting and sporadically erupting volcanoes (Andres and
Kasgnoc, 1998) and for explosive volcanic eruptions (Halmer et al., 2002).

Aerosol number concentrations are treated prognostically with the GLOMAP multi-modal scheme (Mann et al., 2010,
2012), which uses five log-normal aerosol size modes and includes sulfate, sea-salt, black carbon and organic carbon chemical
155   components that are internally mixed within each size mode. Mineral dust is simulated separately using the CLASSIC dust
scheme (Woodward, 2001). GLOMAP simulates new particle formation, coagulation, gas-to-particle transfer, cloud
processing and deposition of gases and aerosols. The activation of aerosols into cloud droplets is calculated using distributions
of sub-grid vertical velocities based on available turbulent kinetic energy (West et al., 2014) and the removal of cloud water
by autoconversion to rain is calculated by the host model. Aerosols are also removed by impaction scavenging of falling
160   raindrops according to the collocation of clouds and precipitation (Lebsock et al., 2013; Boutle et al., 2014).

We modified some aspects of UKESM1-A and perturbed key parameters related to these uncertain processes in the
PPE. Firstly, we defined an ice mass fraction threshold (cloud_ice_thresh; SI table S1) above which no nucleation scavenging
occurs, to allow sufficient aerosol to be transported to the Arctic (Browse et al., 2012). We assumed that the wet scavenging
of all aerosol particles (soluble and insoluble) is zero in large-scale raining clouds if the simulated ice to total water mass
165   fraction is higher than this fixed value. This first structural change replicated the model change we implemented in (Yoshioka
et al., 2019) which is not yet in the release version of the model. We evaluated the climatic importance of this parameter as a
cause of ΔF_{aer} uncertainty in Regayre et al., (2018, 2020), Johnson et al., (2020) and Peace et al., 2020). Secondly, we
implemented a version of look-up tables for aerosol optical properties (Bellouin et al., 2013) that includes optical properties
for mineral dust (Balkanski et al., 2007) and higher-resolution increments of the imaginary part of the refractive indices, to
170   better resolve the absorption coefficient of aerosols. Finally, we included an organically-mediated boundary layer aerosol
nucleation parametrisation (Metzger et al., 2010) to enhance remote marine and early-industrial aerosol concentrations in the
model.

2.1.2 Perturbed parameter ensembles

We created a new PPE of 221 model simulations for this study. Each member of the PPE has a distinct combination of 37
175   aerosol and physical atmosphere parameter values (SI table S1). Parameters perturbed in previous PPEs using older versions
of the model (Yoshioka et al., 2019; Sexton et al., 2021), and identified as important causes of uncertainty in cloud active
aerosol concentrations and/or aerosol forcing (Carslaw et al., 2013; Regayre et al., 2015, 2018), were perturbed here alongside
parameters associated with structural model developments (Mulcahy et al., 2018, 2020; Walters et al., 2019).

We created the PPE in two stages, following 'history matching' conventions (Craig et al., 1997b; Williamson et al.,
180   2013). The main benefit of a multi-stage observational constraint is that it maximises computational efficiency and the value
of information in the final stage PPE by ruling out the most implausible parts of parameter space in earlier stages. We describe

both stages here. However, the second stage PPE is the focus of our analysis. The PPEs in both stages have a ratio of simulations to uncertain parameters of around six to ensure the ensembles accurately represent model responses across the 37-dimensional parameter space.

185   In the first stage, the 221 member ensemble was made by combining a simulation using median values for each parameter with 220 additional parameter combinations drawn from a Latin hypercube optimized to ensure design points were distributed as evenly as possible across the parameter space, using the 'optimumLHS' R function (Stocki, 2005). To extend the sample of model simulations from 221 to 1 million model variants, we created statistical Gaussian process emulators (O'Hagan, 2006) that densely sample model parameter uncertainty. We evaluated a single month of model output (May 2015

190   to match nudged wind fields for this stage) and ruled out model variants (parameter combinations) that compared poorly to global and regional mean observations. At this stage, observations included global mean shortwave and longwave top-of-the-atmosphere radiative fluxes from the Clouds and the Earth's Radiant Energy System experiment (CERES) and global mean precipitation amount from version 2 of the Global Precipitation Climatology Project (GCPC). Additionally, we used North Pacific and North Atlantic marine only data between 10° and 60° N for low- and total-cloud fraction from the Moderate

195   Resolution Imaging Spectroradiometer (MODIS) and LWP from the Multi-Sensor Advanced Climatology of Liquid Water Path data set (Elsaesser et al., 2017). We assumed model-measurement comparison errors of 8%, 2%, 30%, 20%, 20% and 40% respectively for these observations.

For the second (final) stage, we identified the model variant closest to the centre of the not-ruled-out parameter space, then iteratively identified 220 additional parameter combinations with the greatest Euclidean distance from existing points,

200   until we had a new and diverse set of 221 members that spanned the uncertain parameter space retained from the first stage. As in the first stage, we created and validated statistical emulators of global mean and regional mean variables, and used these emulators to extend the output from 221 simulations to 1 million model variants.

2.2 Measurements

We evaluated the potential of several types of observations, related to clouds and aerosol-cloud interactions in multiple

205   locations and times of the year, to serve as global mean ΔF_{aer} constraints and refer to them collectively as 'constraint variables'.

2.2.1 Regional mean cloud and radiative properties

We compared physical and radiative properties of clouds derived from MODIS instruments (King et al., 2003) to model output calculated using the Cloud Feedback Model Intercomparison MODIS satellite simulator (Bodas-Salcedo et al., 2011; Saponaro et al., 2020) where available. This simulator minimizes errors in model comparisons to MODIS retrieval data, by recreating as

210   near as possible what the satellite would retrieve given model-simulated atmospheric conditions.

We used MODIS retrievals of liquid water path (LWP), liquid cloud fraction (f_c), cloud optical depth (τ_c) and cloud droplet effective radius (r_e) at 1° by 1° resolution and used τ_c and r_e values to calculate cloud droplet number concentration (N_d). We assumed constant N_d throughout cloud layers, which is a good approximation for stratocumulus clouds (Grosvenor

and Carslaw, 2020; Painemal and Zuidema, 2011), and compared observed N_d to values calculated at model–simulated cloud
215   tops. Additionally, we used outgoing top-of-the-atmosphere shortwave radiative flux (F_{SW}) measurements from the Clouds
and the Earth's Radiant Energy Systems instrument (CERES).

All satellite-derived measurements were degraded to match the model resolution. We then identified regions with high
cloud fraction across the year (SI table S2). We evaluated constraint variables at the regional level, since there are no clear
relationships between aerosol forcing and observations of global mean values (SI Fig. S1). The chosen regions are dominated
220   by stratocumulus cloud, have relatively high multi-model diversity in cloud amount in CMIP6 models (Vignesh et al., 2020),
and are the most important regions for understanding the role of aerosol-cloud interactions (Langton et al., 2021). We only
used values corresponding to model grid boxes with at least 50% ocean coverage in our area-weighted regional mean
calculations.

These constraint variables are defined as monthly mean, annual mean, or seasonal amplitude (difference between
225   maximum and minimum monthly mean values) within each region. So, for each of our six observation types (F_{SW}, N_{d}, f_c, LWP,
τ_c and r_e) we have 70 constraint variables (12 months, annual mean and seasonal amplitude, all over 5 regions), for a total of
420 regional cloud and radiative flux constraint variables.

2.2.2 Hemispheric difference in N_d

230   The contrast between marine N_d in the polluted Northern Hemisphere and relatively pristine Southern Hemisphere (H_d) can
act as a proxy for the difference in N_d between the early-industrial and present-day atmospheres (McCoy et al., 2020). We
calculated H_d as the difference in hemispheric mean marine N_d values, using MODIS τ_c and r_e values, and evaluated 14
constraint variables calculated as annual and monthly means, and the seasonal amplitude.

2.2.3 Transects from stratocumulus- to cumulus-dominated regions

235   Cloud physical and radiative properties are sensitive to changes in aerosol concentrations in regions where
stratocumulus clouds transition into cumulus (Christensen et al., 2020, 2022). We identified transects from stratocumulus- to
cumulus cloud (SI Fig. S2, table S3) and evaluated changes in aerosol and cloud along these transects (July or November for
Northern and Southern Hemispheres respectively) as constraint variables. We refer to these collectively as transect variables.
These transect variables include changes in N_d, r_e, f_c, LWP and aerosol index (AI; the total MODIS aerosol optical depth at
240   550 nm multiplied by the Ångström exponent) along the transects. Additionally, we included ratios of N_d to AI, r_e to N_d, LWP
to N_d and f_c to N_d along each transect as constraint variables. All transect variables were calculated as gradients of linear
relationships between the variable (or ratio of logarithms following McComiskey et al., 2009) and distance (in meters).

Meteorological covariability (changes induced in both variables by shared meteorological drivers) means that these
transect variables cannot be used to directly infer the strength of the aerosol effect on clouds (Gryspeerdt et al., 2016), but this
245   is not what we do here. Rather, in order to constrain ΔF_{aer}, it is only required that the transect variables (calculated identically

from the observations and model) share causes of uncertainty and parameter dependencies with uncertain parameters in the model (see Sect. 2.3). In total, we evaluated 36 transect variables calculated using 4 transects from stratocumulus- to cumulus-dominated regions.

2.3 Relative importance of parameters

250 One way to prioritise which observations to use for constraint is to quantify the overlap in causes of uncertainty between ΔF_{aer} and model variables associated with the observations (e.g. Regayre et al., 2020). Variance-based sensitivity analyses (Lee et al., 2012) can be used to robustly quantify the percentage of variance caused by each parameter. However, the multi-stage design of the present PPE leaves gaps in the parameter space that limits the interpretability of variance-based methods. Therefore, we approximated the relative importance of parameters as causes of uncertainty using Pearson partial correlations 255 (Kim, 2015). Partial correlations control for the effects of all other perturbed parameters on the variable of interest in the calculation of correlations. A partial correlation between a constraint variable and a parameter is the correlation between the residuals from a) linear regression of the variable on the remaining 36 parameters and b) linear regression of the parameter on the remaining 36. For each of the 37 model parameters we defined the relative importance metric as the proportion of its partial correlation with the variable to the total of the 37 partial correlations, multiplied by the sign of the gradient of the linear 260 regression of the variable on the parameter in question. We included the sign of the gradient to define whether increasing the parameter value increases or decreases the output variable, which helps to develop a process-based understanding. Relative importance metrics are used in section 3.2 to guide our choice of variables for model constraint and to inform our understanding of how they relate to ΔF_{aer}. The metrics were calculated using 1 million model variants (from the emulator) for ΔF_{aer}, and its components from aerosol-cloud interactions (ΔF_{aci}) and aerosol-radiation interactions (ΔF_{ari}), and using the 221 PPE members 265 for other variables.

2.4 Constraint process

2.4.1 Observationally plausible model variants

In our previous effort to constrain ΔF_{aer}, we calculated 'implausibility metrics' that quantify the implausibility of each model variant for all observed values, accounting for emulator uncertainty, observational uncertainty, inter-annual variability and representation errors (Johnson et al., 2020; Regayre et al., 2020). Implausibility metrics were calculated for 1 million model variants across more than 9000 distinct measurements and we used these implausibility values to rule out model variants as observationally implausible if they did not compare well to the full set of observations. In practice, observations associated with relatively large uncertainties had little-to-no impact on ruling out model variants. Using this approach, we constrained ΔF_{aer} and the parameter space, but could not readily isolate the role of individual constraint variables on the resulting ΔF_{aer} 275 constraint and could not quantify how the constraint improved model skill, only how it reduced ΔF_{aer} uncertainty range.

We did not include (largely unquantified) observational errors in our constraint here because we compare satellite data to model output from satellite simulators, which significantly reduces the importance of this source of uncertainty in observation to model comparisons. We also neglected the effects of representation errors (Schutgens et al., 2017) because they are unquantified for the satellite-derived observations used here. Instead, we restricted our model-measurement comparisons to monthly mean values within stratocumulus-dominated regions to reduce the magnitude of these errors. Neglecting observational and representation errors risks over-constraining the model. To avoid over-constraint, we retained a proportion of model variants (at least 5000, or 0.5%) of the same order of magnitude as earlier constraint efforts that used constraint variables with more readily quantifiable sources of model-observation comparison uncertainty (Johnson et al., 2020; Regayre et al., 2020). In this way, our method avoids over-constraining the model, yet allows us to identify potential model structural inconsistencies.

2.4.2 Model-observation differences

We calculated the root mean squared error (RMSE) for each of the 1 million model variants and for each of the 450 constraint variables. For each constraint variable, we then normalized the million RMSE values and ranked model variants according to their normalized RMSE (NRMSE) values to identify which model variants to rule out as least skilful. To further avoid over-constraint, we set NRMSE to zero where the uncertainty in the emulators was large relative to the difference between observed and emulated values. In this way, individual constraints are stronger for constraint variables where parameter perturbations clearly define the response surface of the associated statistical emulators. For this step, we defined the emulator uncertainty as the square root of the emulator variance at that specific combination of model parameters. Thus, for each constraint we retained the larger of either a) all model variants with errors smaller than the emulator uncertainty, or b) the 5000 model variants with the lowest NRMSE. For combinations of constraint variables, we calculated the average NRMSE across all variables for each model variant prior to ranking and rejecting model variants with the highest average NRMSE across variables.

2.4.3 Emulator uncertainty

Constraint variables where the emulator uncertainty (average emulator standard deviation) was larger than the changes in the emulated response surface (standard deviation of emulated values) were removed from our analysis. This was the case for a small number of transect constraint variables and for the seasonal amplitude of f_c in the Southern Ocean. Additionally, we removed transect measurements from the set of constraint variables where the observed values were outside the 90% credible interval of corresponding values in the sample, since such discrepancies are indicative of structural model inadequacies and/or unaccounted for observational errors (SI Fig. S3-6). In total, we evaluated 1 million model variants against the remaining 450 constraint variables.

2.4.4 Internally consistent constraint variables

We identify a subset of the 450 constraint variables that are "pairwise consistent" with N_d in each region. We defined a variable as being consistent with N_d when the constraint to match N_d did not increase the mean NRMSE calculated across the remaining model variants in the associated region and vice versa. We used individual monthly mean N_d values (September,
310 October, December, March and the annual mean for the North Atlantic, North Pacific, South Atlantic, South Pacific and Southern Ocean respectively) to identify which constraint variables could be considered regionally pairwise consistent. These months were chosen based on the degree of between-month N_d-consistency in each region (see Sect. 3.3.2 and SI Fig. S7-10). We assumed constraint variables that are consistent with N_d in these specific months in these regions are also consistent with N_d (and other selected constraint variables) in other regions. Our strategy here is to rule out constraint variables that are clearly
315 inconsistent, rather than to assure internal consistency between all remaining constraint variables. Across all regions, 225 constraint variables were identified as pairwise consistent with N_d.

2.4.5 An optimal set of constraint variables

An "optimal" set of constraint variables was identified (using our specified set of observations and ensemble of model variants) by first identifying the individual constraint variable (from the 225 member N_d-consistent set) with the greatest impact
320 on ΔF_{aci} uncertainty (our target model variable), then progressively adding constraint variables that most improved the overall constraint (quantified as a reduction in the 90% credible interval). That is, we identified the most effective constraint variable, then quantified the constraint efficacy of the remaining 224 variables in combination with the first, and repeated until ΔF_{aci} could not be not constrained further. To avoid confusing a local maximum constraint with an optimal constraint, we continued to add constraint variables to the optimal set, progressively including constraint variables that weakened the ΔF_{aci} constraint
325 the least. At each of the more than twenty thousand steps in this process, we evaluated the average NRMSE values for each of the 1 million model variants, for every possible additional constraint.

We tested the how the order of introducing constraint variables affects the results, since a stronger constraint may be achieved using a different set of "optimal" constraint variables. We could not feasibly calculate NRMSE values for 1 million model variants across all possible combinations of 225 N_d-consistent constraint variables. Instead, we tested the effect of
330 starting with all 225 consistent constraint variables and progressively removing one variable at a time. This is the most distinct test of reordering the constraint variables. This approach yielded a similar "optimal" constraint on ΔF_{aer} as achieved by progressively adding constraint variables (see Sect. 3.3.2) and very similar constraints on marginal parameter distributions (see Sect. 3.3.4 and SI Fig. S11, S12). Additionally, we tested the impact of our choice to retain 5 thousand model variants at each step in the constraint process. The number of constraint variables needed to optimally constrain ΔF_{aer} does vary with the
335 number of model variants retained (SI Fig. S13 and table S4), because reducing the efficacy of individual and combined constraint variables affects the potential for additional observations to further reduce the ΔF_{aci} uncertainty. However, the

strength of constraint and the bounds of constrained ΔF_{aer} are insensitive to the number of model variants retained (SI Fig. S13 and table S4).

3 Results

340   ### 3.1 Sampling uncertainty in ΔF_{aer}

Industrial period ΔF_{aer} ranges from around -3.5 to 3.0 W m^{-2} in our set of 1 million UKESM1-A model variants, with a 90% credible interval of -1.8 to 0.9 W m^{-2} (Fig. 2). This unconstrained 90% credible range (2.7 W m^{-2}) is as wide as the credible range (2.8 W m^{-2}) based on an in-depth review of evidence from models and observations related to aerosol-cloud and aerosol-radiation interactions (Bellouin et al., 2020), and therefore spans a wide spectrum of model behaviour. The range includes

345   positive ΔF_{aer} values that stem from positive forcing contributions from ΔF_{aci} and ΔF_{ari} (SI Fig. S14), which the Bellouin review discounts (Bellouin et al., 2020). These positive ΔF_{aci} and ΔF_{ari} values arise from individually plausible parameter values that produce seemingly implausible model output when combined. As shown below, the associated model variants are amongst those ruled out as observationally implausible.
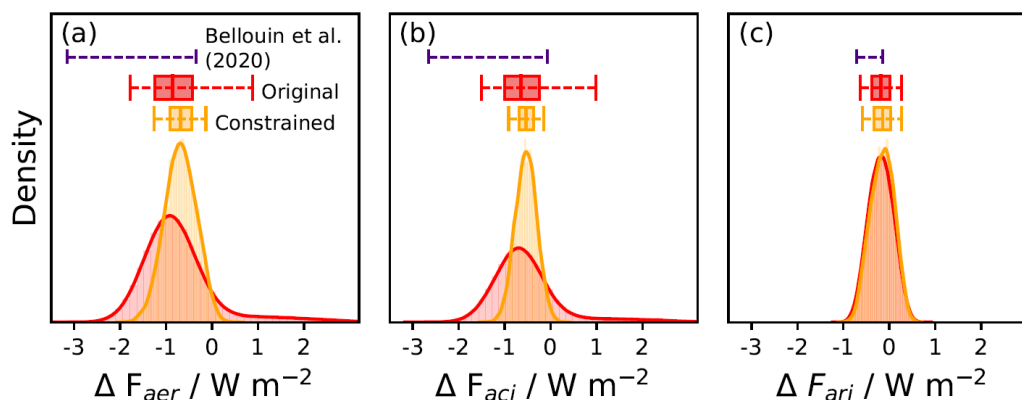
350   **Figure 2. Probability density functions for global, annual mean effective radiative forcings from 1850 to 2014. a) ΔF_{aer}, b) ΔF_{aci} and c) ΔF_{ari} in the original 1 million member sample and after optimal constraint (see Sect. 3.3.2). Box plots show the 5th, 25th, 50th, 75th and 95th percentiles. The 5th and 95th percentiles from Bellouin et al., (2020) are also shown.**

355   ### 3.2 Shared causes of uncertainty and the potential for observational constraint

Our aim is to constrain ΔF_{aer} as tightly as possible using a set of observations that constrain all processes and associated model parameters that cause ΔF_{aer} uncertainty. Figure 3 shows global mean ΔF_{aer} is sensitive to around 10 model parameters (see Sect. 2.3 and SI table S1). Here, we prioritise the constraint of global mean ΔF_{aer} because it is the quantity most commonly

used to inform policy decisions (Forster et al., 2021). We are particularly motivated to constrain processes that cause

360   uncertainty in ΔF_{aci}, since it is the larger and more uncertain component of ΔF_{aer} (Fig. 2) and the ΔF_{ari} component can be more readily constrained using available aerosol observations (Johnson et al., 2020; Watson-Parris et al., 2020). Thus, we seek model variables that share causes of uncertainty with global mean ΔF_{aer} and ΔF_{aci}. Sharing causes of uncertainty (or parameter sensitivity) with ΔF_{aer} is a necessary, but not sufficient, condition for constraint (Lee et al., 2016). Model variables and ΔF_{aer} must also share parameter dependencies (responses to high-dimensional parameter combinations). It is highly unlikely that

365   any one model variable will share exactly the same set of dependencies on uncertain model parameters with ΔF_{aer} and ΔF_{aci} (Lee et al., 2016; Regayre et al., 2020). Thus, to constrain model uncertainty we anticipate needing multiple observations that share at least some causes of uncertainty and parameter dependencies with ΔF_{aer} and ΔF_{aci}.
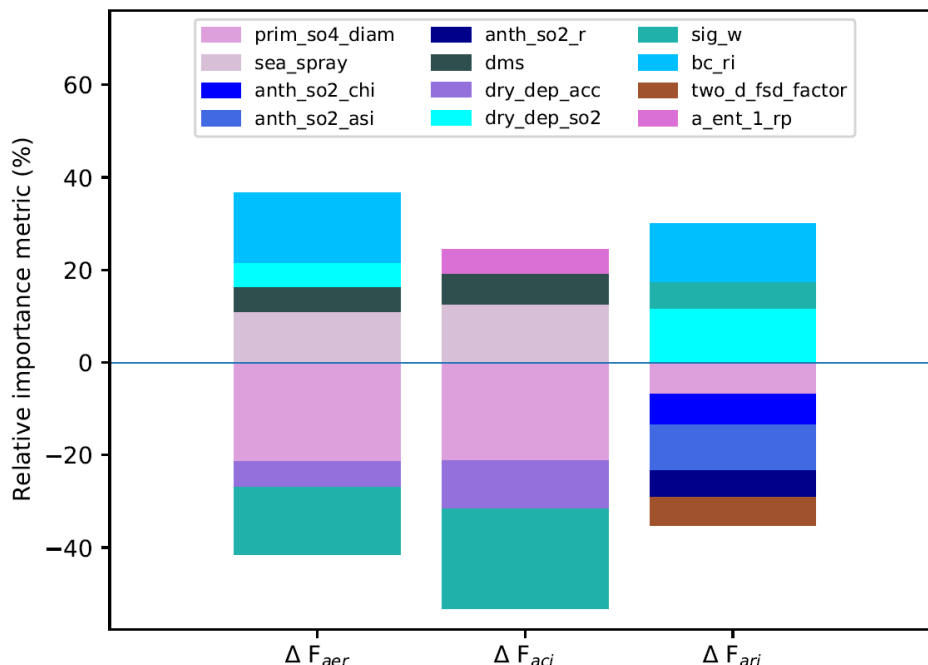
Figure 3: Relative importance of model parameters as causes of uncertainty in global mean ΔF_{aer} and its components

370   **ΔF_{aci} and ΔF_{ari}. Only parameters with a relative importance of 5% or larger are shown. Positive values correspond to parameters where increasing the parameter value causes median values of ΔF_{aer}, ΔF_{aci} or ΔF_{ari} to become weaker (less negative) across the set of 1 million model variants.**

To find a set of useful constraint variables (i.e. a set that collectively share causes of uncertainty and parameter

375   dependencies with ΔF_{aer}), we evaluate a diverse set of constraint variables. Causes of uncertainty and the dependence of forcing on these causes are likely to vary regionally and seasonally (Regayre et al., 2015), so observations of the same type over multiple regions and months may all inform the constraint, but with some redundancy where sensitivities and dependencies

are similar. In total, we have more than 450 constraint variables (see Sect. 2.2) spanning monthly mean, annual mean and seasonal amplitudes, for global mean H_d and 6 observation types (F_{SW}, N_d, f_c, LWP, τ_c and r_e) across 5 stratocumulus-dominated

380   regions (state variables), along with 9 constraint variables for changes in aerosol and cloud properties, and their relationships, each along 4 transects from stratocumulus- to cumulus-dominated regions (transect variables).

First, we evaluate the causes of uncertainty in ΔF_{aer} and its components (Fig. 3). There is substantial overlap between the parametric causes of uncertainty in ΔF_{aer} and ΔF_{aci}, with the parameter that controls the diameter of newly formed accumulation mode sulfate particles ("prim_so4_diam") causing the largest amount of uncertainty. Increasing the value of this

385   parameter increases the diameter of newly emitted sulfate particles and thus decreases the number of particles emitted (for fixed emission mass flux), which makes ΔF_{aci} more negative (stronger) on average since larger particles are more likely to act as cloud condensation nuclei. Any constraint that rules out the most positive ΔF_{aci} values will likely constrain newly formed sulfate particles towards higher diameters.

Other key causes of ΔF_{aer} uncertainty include the parameters controlling sub-grid updraft velocities (sig_w), emission

390   fluxes of sea spray aerosol (sea_spray) and dimethyl-sulfide (dms), the dry deposition removal rate of accumulation mode aerosol (dry_dep_acc), the refractive index controlling carbonaceous aerosol radiative properties (bc_ri) and anthropogenic SO_2 emission fluxes (anth_so2_r). The physical atmosphere parameter controlling cloud top entrainment (a_ent_1_rp) affects ΔF_{aci} uncertainty and the parameter controlling sub-grid cloud heterogeneity (two_d_fsd_factor) affects ΔF_{ari}. However, in contrast with previous PPE analyses of this kind (Regayre et al., 2018; Yoshioka et al., 2019), no physical atmosphere

395   parameters feed through to causes of global mean ΔF_{aer}, likely due to model structural developments related to clouds and radiation (Walters et al., 2019; Williams et al., 2018).

We understand how the key causes of uncertainty affect ΔF_{aci} in the model. Increasing the value of the updraft parameter increases N_d, particularly in the present-day atmosphere with relatively high cloud condensation nuclei concentrations where droplet activation is limited by vertical velocity. Thus, increasing the value of the updraft parameter makes median ΔF_{aci} more

400   negative (stronger) by increasing cloud albedo, particularly in the relatively polluted present-day atmosphere. The influence of natural emission flux parameters on ΔF_{aci} uncertainty is well established (Carslaw et al., 2013). Increasing sea spray or dimethyl-sulfide emission fluxes makes global mean ΔF_{aci} less negative (weaker) on average by increasing the background aerosol concentration and thus reducing the sensitivity of cloud albedo to anthropogenic aerosol. The removal rate of accumulation mode aerosol similarly affects background aerosol concentrations. These three parameters also influence present-

405   day N_d in relatively low anthropogenic aerosol environments such as the Southern Ocean (Hamilton et al., 2014) so can be collectively constrained using appropriate observations (Regayre et al., 2020). However, compensating errors in aerosol emission fluxes and removal rates moderate our ability to constrain these parameters individually (Regayre et al., 2020).

The constraint variable that shares most causes of uncertainty with ΔF_{aer} and ΔF_{aci}, is H_d, the hemispheric difference in marine N_d. The key parameters that cause uncertainty in ΔF_{aci} (related to vertical velocities and sea spray emissions) also cause

410   most of the uncertainty in H_d in all months (Fig. 3 and SI Fig. S15). This suggests we may extract much of the potential constraint from this type of observation using a single representative month (with dependencies on key parameters most closely aligned to ΔF_{aci} parameter dependencies). Other important parameters (newly formed sulfate diameters, DMS emissions and dry deposition velocities) also cause H_d uncertainty in some months. Seasonal differences in causes of H_d uncertainty can be traced to regional causes of N_d uncertainty (not shown), so based on shared causes of uncertainty, both H_d and regional N_d

415   observations have potential to constrain ΔF_{aci}.

Several other observable state variables share key causes of uncertainty with ΔF_{aci} (SI Fig. S16-21). Vertical velocities cause uncertainty in r_e and τ_c (around 20 to 30%), as do dry deposition velocities and, to a lesser extent, newly formed sulfate diameters (around 5 to 10%). Some transect variables also share causes of uncertainty with ΔF_{aci} (SI Fig. S22-25). For example, along the North Atlantic transect, the diameter of newly formed sulfate particles causes up to 50% of the uncertainty in many

420   transect variables, including variables associated the cloud albedo response (gradient of the relationship between r_e and N_d for given LWP) and cloud adjustments (LWP and f_c vs. N_d). Vertical velocities cause up to 35% of the uncertainty in these cloud-related variables in the South Atlantic, whilst dry deposition causes up to 30% in the South Pacific. These regionally distinct causes of uncertainty suggest that observations from transects in several regions may constrain the model when combined, even if each transect variable constrains just one source of parametric uncertainty. Additionally, the radiative properties of

425   carbonaceous aerosol (an important cause of ΔF_{ari} uncertainty) causes around 20% of the uncertainty in several variables along transects in the North Pacific. Thus, North Pacific transect variables have potential to constrain a process related to ΔF_{aer} through ΔF_{ari} that is otherwise unconstrained by our set of satellite-derived observations. In contrast with model constraint efforts designed to improve model skill more generally (Sexton et al., 2012), our evaluation of shared causes of uncertainty provides process-based insight into the nature of any ΔF_{aer} constraint we may achieve.

430   Not all state variables share causes of uncertainty with global mean ΔF_{aer} and ΔF_{aci}. Outgoing radiative flux (F_{SW}) shares a few causes of uncertainty with ΔF_{aci} but is largely controlled by physical atmosphere parameters (in agreement with Regayre et al., 2018). Similarly, global mean f_c and LWP share only a few minor causes of uncertainty with ΔF_{aci}, with values for these variables predominantly controlled by physical atmosphere parameters and uncertainties in the autoconversion scheme (that converts cloud drops to rain drops). Yet at the regional level (not shown), key parameters like the updraft

435   parameter contribute between 5 to 10% of the f_c and LWP uncertainty in most months, so f_c and LWP observations may still influence the ΔF_{aci} constraint. Thus, although some observation types have far greater potential for ΔF_{aci} constraint than others (based on shared causes of uncertainty) we do not exclude any from our constraint process at this stage. The overlap in causes of uncertainty across constraint variables suggests that in practice, we may only need a subset to constrain ΔF_{aer} and others will be effectively redundant.

3.3 Observational constraint

3.3.1 Detection of potential structural model inadequacies

Our goal is to constrain parametric uncertainty in ΔF_{aci}, ideally using all of the available observations, but in practice using a subset of observations for which the model-observation comparison is not affected by structural model inadequacies. We use two key indicators to identify potential structural model inadequacies. Firstly, some observations lie outside the range of the 1 million model variants, or are amongst the most extreme values. This indicates a discrepancy between the model and the observations that adjustments to model parameters cannot overcome (even by adjusting multiple parameter values simultaneously). That is, the discrepancy is more likely caused by a structural model deficiency than by parametric uncertainty. In practice, the discrepancy between model values and observations may be caused by very large, unquantified observational uncertainties or their lack of spatiotemporal representativeness (Schutgens et al., 2017). In such cases, either the model is incorrect due to some structural error, or the observation is unreliable. Variables associated with this type of indicator are not useful for model constraint. Secondly, constraint of the model using observations related to some constraint variables can degrade model skill at simulating other variables (Johnson et al., 2020; McNeall et al., 2016; Sengupta et al., 2021). In such cases, the model can be constrained towards one set of constraint variables or another, but not both simultaneously without systematically weakening the constraint. This suggests structural inadequacies prevent the model from consistently representing all processes associated with these constraint variables.

We begin by analysing potential structural errors in just one stratocumulus-dominated region. Fig. 4 shows the seasonal cycles of cloud physical and radiative properties in the North Atlantic (for other regions see SI Fig. S26-29). The distribution of the 1 million model F_{SW} values is centred on observed values, which is expected since extensive evaluations of F_{SW} across multiple model configurations feed into the model development process. Similarly, the distribution of f_c values is centred on the observations, with the exception of the April observation. This suggests that the f_c observation for April may be corrupted, or affected by some atypical event the model did not simulate, so should probably not inform our constraint. Model variants generally overestimate N_d, although N_d observations are well within the model's parametric uncertainty range. For LWP, τ_c and to a lesser extent r_e, observed values are near the edge of the model parametric uncertainty range or outside the range by a small margin. We have accounted for a very wide range of parameter uncertainties, but cannot adequately reproduce observed LWP and τ_c values in this region (more extreme in other regions and for some transect variables; SI Fig. S3-6; S26-29), which suggests the model bias is caused by some structural deficiency. We cannot rule out satellite retrieval biases as an explanation for the model-observation bias with this first type of indicator, but the distinction between model structural error and observation error is not important in terms of model constraint. We therefore refer to such biases as *potential* structural inadequacies and remove the associated constraint variables from our process. Figure 4 exemplifies how we can compare observations to a broad range of model output to identify potential structural inadequacies where only extreme model behaviour aligns with observations.

We identified instances of the second indicator of potential structural inadequacy (associated with inconsistent model process representations) by evaluating how constraint of each model variable affects all other variables. We call this "pairwise" comparison. Figure 4 shows two contrasting sets of pairwise comparisons, highlighting both consistency and inconsistency.

475 We constrained the model to match the mean N_d observation for November in the North Atlantic and, separately, to match November LWP observations in this region. November was chosen to exemplify the effect of the second indicator of potential structural inadequacy because the parametric uncertainty in N_d and LWP peaks in this month. In each case we ruled out model variants with relatively large model-observation differences (quantified using NRMSEs) as observationally implausible and retained the subset of model variants with values closest to observations (Sect. 2.4.5). Individual constraint variables have a

480 large effect on the uncertainty of the same observation type in other months because they share common causes of uncertainty in the model. For example, constraint to November N_d consistently reduces N_d uncertainty in all other months and brings the remaining model variants into close agreement with measured N_d values. This set of model variants also closely match F_{SW} and f_c observations, with the exception of April f_c, which we have already identified as problematic.

These pairwise comparisons suggest that representations of N_d, F_{SW} and f_c are internally consistent in the model and we

485 may only need a subset of these constraint variables to reduce uncertainty in ΔF_{aer}. However, the set of N_d-constrained model variants do not span the LWP, τ_c or r_e observations in most months, suggesting that model N_d is inconsistent with LWP, τ_c and r_e over the North Atlantic. In the other constraint shown in Fig. 4, the model variants that are consistent with November LWP in the North Atlantic do not span F_{SW}, f_c or r_e observations. Retrievals of cloud properties are consistent by design due to dependencies in their calculation. That is, multiple retrieved cloud properties from the same instrument share causes of

490 observation bias. Thus, our results suggest structural deficiencies in the model related to internal inconsistencies in the representations of physical and radiative cloud properties, which may be caused by the use of a single-moment cloud microphysics scheme in UKESM1. For example, in a single-moment microphysics scheme where N_d is not prognosed, removal of cloud water in precipitation (affecting LWP and τ_c) does not act consistently on N_d, which is prescribed by aerosol activation at cloud base. Using a double-moment microphysics scheme, such as the Cloud–AeroSol Interacting Microphysics (CASIM)

495 scheme (e.g. Grosvenor and Carslaw, 2020; Grosvenor et al., 2017; Hill et al., 2015; Shipway and Hill, 2012; Gordon et al., 2018), that simulates cloud water (droplet mass) and droplet number in a more-realistic way could eliminate these internal model inconsistencies. However, in our ensemble these inconsistencies may prevent us using all available data for constraint of ΔF_{aci}.
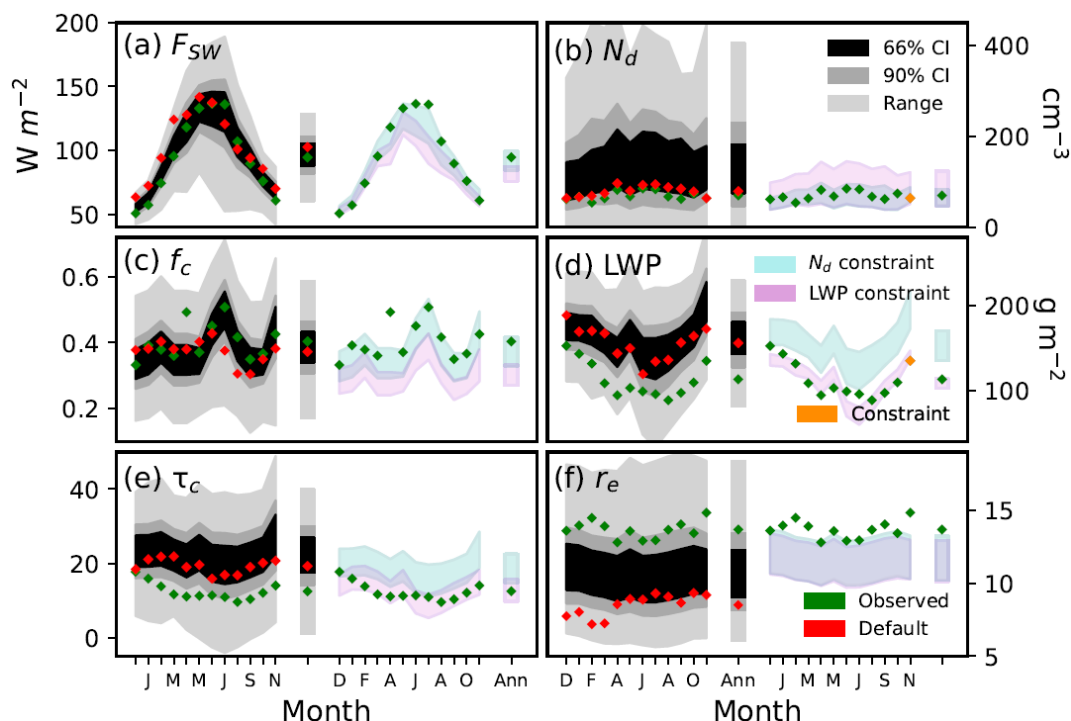
Figure 4: Seasonal cycles of North Atlantic mean radiative fluxes and cloud properties before and after observational constraint using a single month of observations. Model output for individual months spanning December 2016 to November 2017 are followed by the annual mean. Credible intervals for the full set of model variants are shown (grey shading) along with satellite-derived observations and the default UKESM1-A model values. Each panel also shows the range (shading) of values from the November N_d constraint (green) and the November LWP constraint (pink; arrows show constraint variable). The orange data point shows the observed variable and month used for the constraint.

To reveal the full extent of internal model consistencies and inconsistencies, we extended the analysis in Fig. 4 to all pairwise comparisons of the 88 North Atlantic constraint variables and 14 H_d constraint variables (Fig. 5; other regions are shown in SI Fig. S7-10). Calculation of each of these pairwise effects across the full parameter space requires 1 million model-to-observation comparisons for each variable that is constrained and another million for each variable being compared. Two constraint variables are judged to be pairwise consistent if constraint to one variable improves the model–observation comparison for the other variable and vice versa. We quantify the impact on model-observation comparison as the percentage change in the average NRMSE, when moving from the unconstrained set of 1 million model variants to the set of model variants retained by the constraint (Sect. 2.4.2). For each pairwise comparison, green shading in Fig. 5 indicates that observational constraint of the variable on the y-axis improves the model-observation agreement (reduces average NRMSE) for the variable on the x-axis. Pink shading indicates that the average NRMSE increases, which suggests that the two variables are inconsistent – that is, the set of model variants that best match the variable on the y-axis are on average further from

observations related to the variable on the x-axis than in the original (unconstrained) set. For example, model skill at simulating April f_c declines after constraint of any other variable, even f_c in most other months (vertical pink stripe). This supports our

520 hypothesis that an observational error is the cause of the April f_c discrepancy and rules out using this constraint variable. These pairwise comparisons of constraint effects reveal inconsistencies between model variables LWP, τ_c and r_e, and other variables related to cloud properties (F_{SW}, N_d and f_c) in the North Atlantic (top right quadrant and bottom right panel of Fig. 5) and other regions (SI Fig. S7-10).
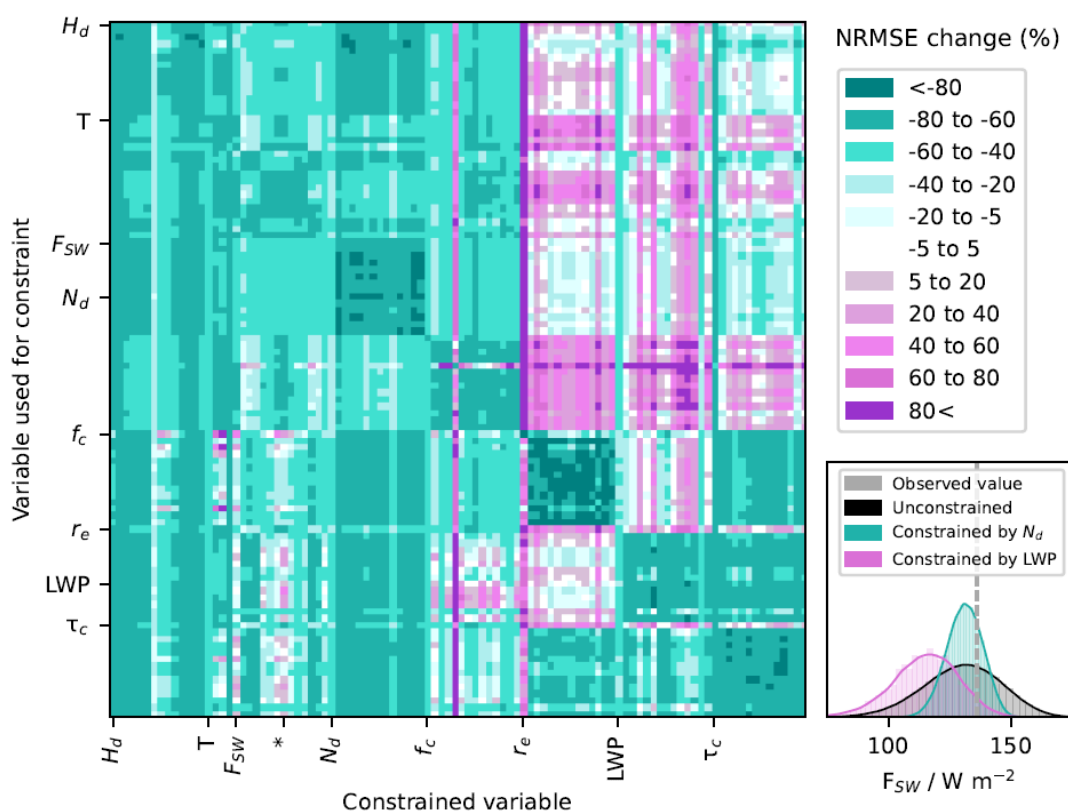
525 **Figure 5: Pairwise comparisons of North Atlantic constraint variables (and hemispheric difference, H_d) showing how constraint of one variable affects all others. The y-axis labels refer to variables used to constrain the model output and the x-axis labels refer to variables whose values have been consequently constrained. For each state variable, the pixels in the first row/column are the seasonal amplitude, followed by individual months from January to December and the annual mean. Transect variables are within the section labelled "T". Shading indicates the percentage change in**
530 **average NRMSE after constraint. In the bottom-right panel we exemplify the effect of constraint on average NRMSE in one pixel in terms of probability density functions of July F_{SW} in the unconstrained set of model variants (black), in the set constrained to match July N_d observations (green), and in the set constrained to match July LWP (pink).**

3.3.2 Optimal constraint of aerosol forcing

The pairwise comparisons in Fig. 5 show that it is not appropriate to use all observed variables to constrain the model because,
due to potential structural model inconsistencies, different variables are consistent with different combinations of model
parameters. The set of variants that simultaneously encompasses as many observed variables as possible is essentially the full
initial set of 1 million. However, a smaller set of variants could be identified that agree with those observed variables that are
represented consistently in the model. This is an approach taken either deliberately or inadvertently in model tuning in which
some variables are deprioritised or neglected altogether. For example, F_{SW} is almost always treated as a high-priority target
when tuning climate models because of its importance for energy balance, while N_d is more commonly treated as an adjustment
term to achieve greater agreement with target values, and many other cloud variables are often neglected completely (e.g.
Hourdin et al., 2017). Model tuning approaches attempt to minimise the effect of biases in a well-configured model version
rather than seeking to identify structural systematic biases across a large number of model variants as we do here. There is no
agreed best practice for identifying which combinations of model variables are structurally consistent. To explore the potential
for constraint of ΔF_{aci}, we take the approach of constraining to the *most consistent* set of observed variables across our selected
regions, then add more variables to understand the effect of accounting for inconsistencies.

We first identify constraint variables that are pairwise consistent with N_d at the regional level (see Sect. 2.4.4). We
chose the 225 constraint variables that are N_d-pairwise consistent because N_d is one of the most uncertain variables we evaluate
here (Fig. 4), and N_d is a common adjustment variable for ΔF_{aer} constraint (Hourdin et al., 2017) due to its sensitivity to aerosol
and its importance for ΔF_{aci}. In practice, we could use other constraint variables to define an internally consistent set (top left
corner of Fig. 5). We evaluate the 25,200 combinations of these 225 constraint variables to reveal structural inconsistencies
(Sect. 2.4.4). First, we identify the constraint variable with the greatest individual effect on reducing ΔF_{aci} uncertainty, then
progressively add constraint variables that are consistent with the existing set of variables (and N_d at the regional level) and
contribute most to the ΔF_{aci} constraint. Figure 6 shows the effect of progressively adding constraint variables in this way
(orange points).

The hemispheric contrast in N_d (H_d) in the Northern Hemisphere summer (August) provides the strongest individual
constraint on ΔF_{aci}. The constraint towards lower values of H_d in August reduces the credible ΔF_{aci} uncertainty range in the
unconstrained set of model variants by around 44%. August H_d shares causes of uncertainty with ΔF_{aci}, and with H_d in all other
months, but the nature of the relationships between the associated parameters (parameter dependencies) may be more clearly
defined in August, since in most other months H_d is sensitive to additional parameters (SI Fig. S15). In combination with
August H_d, additional constraint comes from next including South Pacific N_d in September (dependencies on natural emission
flux parameters and dry deposition velocity), followed by March H_d (carbonaceous aerosol properties). Further constraint
comes from North Pacific f_c in August (updraft velocity, autoconversion and physical atmosphere parameters) and changes in
LWP along the North Pacific transect (carbonaceous aerosol radiative properties, autoconversion and physical atmosphere

565   parameters). Southern Ocean N_d in December (natural emission fluxes and dry deposition velocities) and changes in LWP and
N_d along the North Atlantic transect (updraft velocity and primary sulfate diameter) additionally constrain ΔF_{aci}.
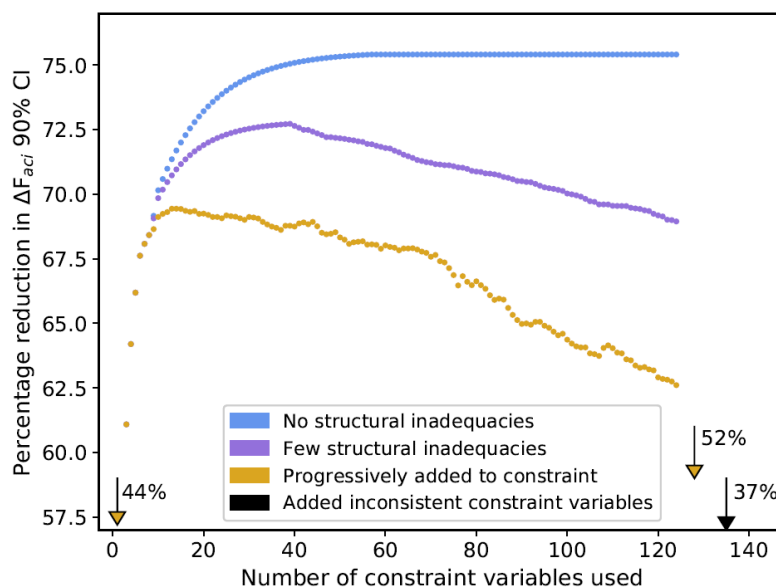
**Figure 6: Constraint of ΔF_{aci} and the effect of varying the number of constraint variables used. We show the effect of
progressively adding constraint variables with the greatest influence on ΔF_{aci} uncertainty (orange), alongside synthetic**
570   **examples of how the constraint might improve with very few, or no structural model inadequacies (purple and blue
respectively). In each case, only the first 125 of 225 N_d-pairwise consistent constraint variables are shown. Arrows
indicate the constraint of ΔF_{aci} using the single strongest constraint (44%), all 225 N_d-pairwise consistent constraint
variables (52%) and all 450 constraint variables (37%), including those associated with identified structural
inadequacies at the regional level (e.g. Fig. 4 and 5).**

575   We only need to include 7 additional constraint variables, in combination with the constraints identified above, (13 in
total) to optimally constrain ΔF_{aci} (i.e. greatest reduction in the ΔF_{aci} 90% credible interval, orange points in Fig. 6). We define
the "optimal constraint" to be the greatest reduction in ΔF_{aci} achievable using our specified set of observations and structurally
imperfect model. This optimal set of constraint variables spans the observation types, regions and seasons, and provides
information about the key uncertain parameters associated with these observations (and ΔF_{aci} dependencies on key model
580   parameters). The optimally constrained set of model variants reduces ΔF_{aci} uncertainty by nearly 70% (90% credible interval
-0.9 to -0.1 W m^{-2}) and ΔF_{aer} uncertainty by more than 50% (-1.3 to -0.1 W m^{-2}; Fig. 2). This constrained ΔF_{aer} range is
narrower than previous best estimates (Bellouin et al., 2020) and purely process-based constraints (Regayre et al., 2018, 2020;
Johnson et al., 2020) even though the ΔF_{ari} component of forcing is effectively unconstrained here. Additionally, the optimally
constrained lower negative bound is now in close agreement with energy-balance constraints (table 1).

585   When applied in combination with the set of the 13 optimal constraint variables, any additional variables weaken the constraint (Fig. 6). This is because the additional variables are inconsistent with those already used. We retain at least 5 thousand model variants for each combined constraint (Sect. 2.4.1), so the result of adding further observations is a compromise in the sense that the existing constraints of ΔF_{aci} dependencies on key parameters need to be relaxed to accommodate conflicting information introduced by inconsistent variables. Practically, this means that some of the model variants with low

590   NRMSE values are no longer retained. Instead, these model variants are replaced with other variants that have tolerable (not low) NRMSE values for the existing set of constraint variables *and* tolerable NRMSE values in relation to the new variable. Thus, the constraint is no longer optimal (for our model and these observations). Including all 225 observations of N_d-pairwise consistent constraint variables reduces the ΔF_{aci} uncertainty by just over 50%, and adding observations of inconsistent variables to the constraint reduces the uncertainty by less than 40%. We expected a decline in constraint efficacy (levelling off when

595   progressively adding constraint variables; Fig. 6) once hidden structural inconsistencies started to mitigate the benefits of including additional constraint variables. However, we did not anticipate the optimal constraint to include so few constraint variables. These results suggest across 1 million variants, the model is structurally incapable of matching more than a handful of our chosen observations simultaneously (Fig. 6 and SI table S4).

3.3.3 Constraint of uncertain model parameters

600   Our approach consistently constrains the values of model parameters (SI Fig. S11, S12). Most parameters that cause ΔF_{aci} uncertainty (Fig. 3) are constrained, as are numerous other parameters that cause uncertainty in variables associated with our set of optimal observations, that are not shared with ΔF_{aci}. We entirely rule out some values as observationally implausible for parameters related to vertical velocity and newly formed sulfate particle diameters. Vertical velocities are constrained towards lower values, which are consistent with lower N_d concentrations in the relatively polluted Northern Hemisphere, a

605   lower hemispheric contrast in N_d and weaker (less negative) median ΔF_{aci}. Conversely, newly formed sulfate particle diameters are constrained towards higher values, consistent with higher concentrations of cloud active aerosol concentrations and stronger (more negative) median ΔF_{aci}. Low sulfate emission diameters likely contributed to the spurious positive ΔF_{aci} values in Fig. 2. Dry deposition removal rates are also constrained towards higher values. This constraint reduces background aerosol concentration (consistent with lower N_d) and causes stronger (more negative) median ΔF_{aci} (increased sensitivity to

610   anthropogenic aerosol). These key parameters are constrained concurrently, so have the effect of ruling out the strongest *and* weakest ΔF_{aci} (and ΔF_{aer}) values in our original set of model variants.

    There is little evidence to support altering the current model representations of natural emission fluxes. Two key causes of ΔF_{aci} uncertainty, the emission fluxes of sea spray aerosol and DMS are constrained towards central values. However, the constraints on these parameters are relatively modest given their importance as causes of uncertainty. Additional constraint

615   using in situ observations in relatively unpolluted regions (Hamilton et al., 2014; Schmale et al., 2019) could further constrain these parameters and the ΔF_{aci} uncertainty (Regayre et al., 2020). Also, additional ΔF_{aer} constraint could be achieved using in-

situ observations that target processes related to the ΔF_{ari} component of ΔF_{aer} (Johnson et al., 2020; Watson-Parris et al., 2020), which is effectively unconstrained by the satellite-derived observations used here.

Table 1. 90% credible intervals for ΔF_{aer}, ΔF_{aci} and ΔF_{ari} from the original 1 million model variants, and after
620 **constraint using process-based and energy-balance methods. We also include plausible bounds (90% credible interval) from energy-balance constraints.**

	ΔF_{aer} (W m^{-2})	ΔF_{aci} (W m^{-2})	ΔF_{ari} (W m^{-2})
Unconstrained	-1.8 to 0.9	-1.5 to 1.0	-0.6 to 0.3
All constraint variables (450)	-1.5 to 0.2	-1.2 to 0.2	-0.6 to 0.2
N_d-pairwise consistent constraint variables (225)	-1.4 to 0.0	-1.1 to 0.1	-0.6 to 0.3
Optimal set of constraint variables (13)	-1.3 to -0.1	-0.9 to -0.1	-0.6 to 0.3
Smith et al. 2021; 1750 to 2019	-1.5 to -0.4	-1.2 to -0.1	-0.6 to -0.1
Albright et al. 2021	-1.3 to -0.5	-0.9 to -0.2	-1.0 to 0.0

4 Discussion

We illustrate some of the benefits of climate model evaluation that accounts for parametric uncertainty. In addition to
625 constraining the lower bound on ΔF_{aer} to -1.3 W m^{-2}, a value in close agreement with energy-balance constraints, we have shown how this type of model evaluation can reveal potential structural model inadequacies. In our case, prioritising structural improvements to address model inconsistencies related to the representations of cloud variables, would increase the number and type of observations that could be used to further reduce ΔF_{aci} and ΔF_{aer} uncertainty in the model.

Structural inconsistencies weaken model observational constraint because to achieve tolerable agreement with more
630 variables than in the optimal set, the inconsistencies demand a compromise in the tightness of constraint achieved (Fig. 7). In UKESM1-A, the set of optimal constraint variables is surprisingly small, containing only around 3% of the constraint variables we explored. At present, the remaining 97% of variables weaken the optimal constraint. If we could make these variables consistent with the model, for example by altering the structure of the model, then they would instead add to the constraint by further defining parameter relationships that were not constrained by the 3%. The hypothetical lines in Fig. 6 (purple and blue)
635 describe what might be achieved if some or all of the structural model inadequacies were identified and improved – moving the peak to the right (more constraint variables used consistently in a structurally different model) and raising the peak (tighter parametric constraint of ΔF_{aci} and ΔF_{aer}). The values used to create these lines are chosen to exemplify our point and do not correspond to actual constraints of the model. Ultimately, in a model without any structural inadequacies, the constraint versus number of variables would asymptote – additional variables would further constrain parameter relationships that were already
640 partially constrained. The magnitude of constraint at this hypothetical asymptote is currently unknown. It will be determined

in part by the effects of observational uncertainty and model-observation representation errors (Schutgens et al., 2017). Thus, we consider our optimal constraint the *minimum level* of process-based constraint that we might achieve, with this set of observations, if we could eliminate structural model inadequacies.
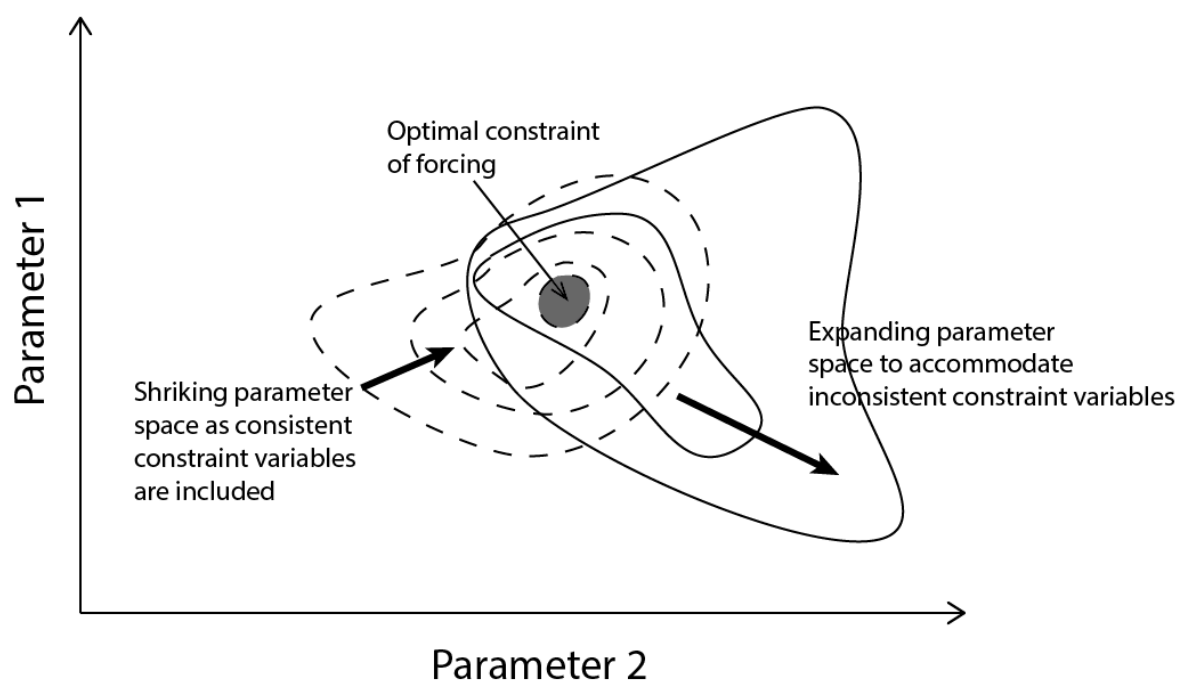
Figure 7: Schematic of how the addition of constraint variables affects the constrained parameter space. This is a 2-dimensional schematic of what is here a 37-dimensional problem. Initially, adding constraint variables leads to a reduction in the amount of parameter space that corresponds to a relatively good match to the observations (rising branch of Fig. 6). Each new variable constrains the parameter space more than the previous set. An optimum constraint is reached (shaded grey region; peak in Fig. 6). Beyond this point, each new constraint variable is no longer consistent with the existing set already used because the model has structural deficiencies. Thus the parameter space must be expanded (and the ΔF_{aer} constraint weakened) to accommodate these inconsistencies.

We suggest modelling groups may benefit from replacing existing model tuning strategies with a new approach to model evaluation and development that accounts for parametric uncertainty and strategically identifies the causes of model inconsistencies as well as ways to overcome their effects. In practice, the magnitude and distribution of observationally constrained ΔF_{aer} values in a structurally improved model may differ from the original model values (even with an identical set of parameter combinations). Thus, coherent progress at improving model skill at simulating aerosol-cloud interactions may require several cycles of uncertainty quantification, constraint, structural error identification and model development. Open source tools and code can help simplify some aspects of model evaluation within an uncertainty framework (Watson-Parris et al., 2021) and thus streamline some aspects of this cycle.

660   Identifying optimal replacements for inconsistent process representations will require additional insight into the causes of uncertainty within and across climate models, although knowledge of inconsistencies between variables provided by our approach will provide a strong steer. This valuable insight could be achieved by extending model intercomparisons, such as the 6th Coupled Model Intercomparison Project (CMIP6; Eyring et al., 2016), to include a cross-model perturbed parameter component. The breadth of model behaviour sampled in enhanced intercomparisons would help to identify optimal
665 combinations of process representations and parameter values that minimise important shared biases in climate models. Additionally, data from such ensembles would be invaluable for training relatively simple climate models (Albright et al., 2021; Smith et al., 2021) and would contribute to efforts to identify robust emergent constraints (Carslaw et al., 2018). Experiments that sample parametric uncertainty *and* structural model differences could help deliver a step change in model skill at making climate projections beyond the advances we have achieved here using a single climate model.

670 **Data availability**

Output from the A-CURE PPE is available on the CEDA archive (Regayre *et al.*, 2022). Python code used in this research is available here: https://github.com/Leighton-Regayre/article_code_constraint_aerosol_ERF.git

Author contributions

LR and KC wrote the article. LR designed the experiments, with input from JJ, KC, PS, LD, DWP, KP and JM. LR, KP and
675 CS implemented code changes for parameter perturbations. JM advised on specific aspects of model set-up associated with aerosols and couplings between model components and LR implemented these changes. DS and JR advised on choice of physical atmosphere parameters to perturb in our ensemble. LR created the first stage ensemble. LR, LD, TL, CS and MR created the much larger second stage ensemble. GL, MD and MR provided technical expertise that assisted with creation of the PPE. LR processed the data, with contributions from DG and HG. LR analysed the data in collaboration with KC, DG, JJ,
680 LD, PS, DWP and DS. LR, KC and JJ developed aspects of the methodology for identifying model structural inadequacies. All co-authors commented on the article.

Competing interests

We have no competing interests to declare.

Acknowledgements

685 LR, KS and PS acknowledge funding from the FORCeS project under the European Union's Horizon 2020 research programme with grant agreement 821205. We acknowledge funding from NERC under grants AEROS, ACID-PRUF, GASSP

and A-CURE (NE/G006172/1, NE/I020059/1, NE/J024252/1 and NE/P013406/1) and the European Union ACTRIS-2 project under grant 262254. DG and KS were supported by the National Environmental Research Council (NERC) national capability grant for The North Atlantic Climate System Integrated Study (ACSIS) program (grant NE/N018001/1) via NCAS and by the

690 NERC ADVANCE Standard Grant project (NE/T006897/1). DWP acknowledges funding from the European Union's Horizon 2020 research and innovation programme iMIRACLI under Marie Skłodowska-Curie grant agreement No 860100. P.S additionally acknowledges funding from the European Research Council (ERC) project constRaining the EffeCts of Aerosols on Precipitation (RECAP) under the European Union's Horizon 2020 research and innovation programme with grant agreement no. 724602. DS was supported by the Met Office Hadley Centre Climate Programme funded by BEIS and Defra.

695 JR was supported by the UK-China Research & Innovation Partnership Fund through the Met Office Climate Science for Service Partnership (CSSP) China as part of the Newton Fund. JPM was supported by the Met Office Hadley Centre Climate Programme funded by BEIS. HG acknowledges support from the NASA Roses program under grant number 80NSSC21K1344. This work used the ARCHER UK National Supercomputing Service (http://www.archer.ac.uk) under project allocation n02-NEP013406 to create the ensemble. KC was a Royal Society Wolfson Merit Award holder during

700 this research. We appreciate expert advice provided by Masaru Yoshioka, Ben Johnson, Alex Archibald, Carly Reddington, Steven Turnock and Cat Scott, which allowed us to adjust uncertain model parameter ranges in light of recent research and model developments. We thank Ananth Ranjithkumar who shared code changes specific to high time-resolution output and Haochi Che who provided carbonaceous aerosol emission files in a model-ready format.

References

705 Albright, A. L., Proistosescu, C., and Huybers, P.: Origins of a Relatively Tight Lower Bound on Anthropogenic Aerosol Radiative Forcing from Bayesian Analysis of Historical Observations, Journal of Climate, 34, 8777–8792, https://doi.org/10.1175/JCLI-D-21-0167.1, 2021.

Aldrin, M., Holden, M., Guttorp, P., Skeie, R. B., Myhre, G., and Berntsen, T. K.: Bayesian estimation of climate sensitivity based on a simple climate model fitted to observations of hemispheric temperatures and global ocean heat content: 710 ESTIMATING CLIMATE SENSITIVITY, Environmetrics, 23, 253–271, https://doi.org/10.1002/env.2140, 2012.

Andreae, M. O., Jones, C. D., and Cox, P. M.: Strong present-day aerosol cooling implies a hot future, Nature, 435, 1187–1190, https://doi.org/10.1038/nature03671, 2005.

Andres, R. J. and Kasgnoc, A. D.: A time-averaged inventory of subaerial volcanic sulfur emissions, J. Geophys. Res., 103, 25251–25261, https://doi.org/10.1029/98JD02091, 1998.

715 Archibald, A. T., O'Connor, F. M., Abraham, N. L., Archer-Nicholls, S., Chipperfield, M. P., Dalvi, M., Folberth, G. A., Dennison, F., Dhomse, S. S., Griffiths, P. T., Hardacre, C., Hewitt, A. J., Hill, R., Johnson, C. E., Keeble, J., Köhler, M. O., Morgenstern, O., Mulchay, J. P., Ordóñez, C., Pope, R. J., Rumbold, S., Russo, M. R., Savage, N., Sellar, A., Stringer, M., Turnock, S., Wild, O., and Zeng, G.: Description and evaluation of the UKCA stratosphere-troposphere chemistry scheme (StratTrop vn 1.0) implemented in UKESM1, Atmospheric Sciences, https://doi.org/10.5194/gmd-2019-246, 2019.

720 Balkanski, Y., Schulz, M., Claquin, T., and Guibert, S.: Reevaluation of Mineral aerosol radiative forcings suggests a better agreement with satellite and AERONET data, Atmos. Chem. Phys., 7, 81–95, https://doi.org/10.5194/acp-7-81-2007, 2007.

Bellouin, N., Mann, G. W., Woodhouse, M. T., Johnson, C., Carslaw, K. S., and Dalvi, M.: Impact of the modal aerosol scheme GLOMAP-mode on aerosol forcing in the Hadley Centre Global Environmental Model, Atmos. Chem. Phys., 13, 3027–3044, https://doi.org/10.5194/acp-13-3027-2013, 2013.

725 Bellouin, N., Quaas, J., Gryspeerdt, E., Kinne, S., Stier, P., Watson-Parris, D., Boucher, O., Carslaw, K. S., Christensen, M., Daniau, A. -L., Dufresne, J. -L., Feingold, G., Fiedler, S., Forster, P., Gettelman, A., Haywood, J. M., Lohmann, U., Malavelle, F., Mauritsen, T., McCoy, D. T., Myhre, G., Mülmenstädt, J., Neubauer, D., Possner, A., Rugenstein, M., Sato, Y., Schulz, M., Schwartz, S. E., Sourdeval, O., Storelvmo, T., Toll, V., Winker, D., and Stevens, B.: Bounding Global Aerosol Radiative Forcing of Climate Change, Rev. Geophys., 58, https://doi.org/10.1029/2019RG000660, 2020.

730 Bodas-Salcedo, A., Webb, M. J., Bony, S., Chepfer, H., Dufresne, J.-L., Klein, S. A., Zhang, Y., Marchand, R., Haynes, J. M., Pincus, R., and John, V. O.: COSP: Satellite simulation software for model assessment, Bulletin of the American Meteorological Society, 92, 1023–1043, https://doi.org/10.1175/2011BAMS2856.1, 2011.

Boutle, I. A., Abel, S. J., Hill, P. G., and Morcrette, C. J.: Spatial variability of liquid cloud and rain: observations and microphysical effects: Cloud and Rain Variability, Q.J.R. Meteorol. Soc., 140, 583–594, https://doi.org/10.1002/qj.2140, 2014.

735 Browse, J., Carslaw, K. S., Arnold, S. R., Pringle, K., and Boucher, O.: The scavenging processes controlling the seasonal cycle in Arctic sulphate and black carbon aerosol, Atmos. Chem. Phys., 12, 6775–6798, https://doi.org/10.5194/acp-12-6775-2012, 2012.

Brynjarsdóttir, J. and O'Hagan, A.: Learning about physical parameters: the importance of model discrepancy, Inverse Problems, 30, 114007, https://doi.org/10.1088/0266-5611/30/11/114007, 2014.

740 Carslaw, K. S., Lee, L. A., Reddington, C. L., Pringle, K. J., Rap, A., Forster, P. M., Mann, G. W., Spracklen, D. V., Woodhouse, M. T., Regayre, L. A., and Pierce, J. R.: Large contribution of natural aerosols to uncertainty in indirect forcing, Nature, 503, 67–71, https://doi.org/10.1038/nature12674, 2013.

Carslaw, K. S., Lee, L., Regayre, L., and Johnson, J.: Climate Models Are Uncertain, but We Can Do Something About It, Eos, 99, https://doi.org/10.1029/2018EO093757, 2018.

745 CERES: https://ceres.larc.nasa.gov/documents/DQ_summaries/CERES_SYN1deg_Ed4A_DQS.pdf.

Christensen, M. W., Jones, W. K., and Stier, P.: Aerosols enhance cloud lifetime and brightness along the stratus-to-cumulus transition, Proc. Natl. Acad. Sci. U.S.A., 117, 17591–17598, https://doi.org/10.1073/pnas.1921231117, 2020.

Christensen, M. W., Gettelman, A., Cermak, J., Dagan, G., Diamond, M., Douglas, A., Feingold, G., Glassmeier, F., Goren, T., Grosvenor, D. P., Gryspeerdt, E., Kahn, R., Li, Z., Ma, P.-L., Malavelle, F., McCoy, I. L., McCoy, D. T., McFarquhar, G.,
750 Mülmenstädt, J., Pal, S., Possner, A., Povey, A., Quaas, J., Rosenfeld, D., Schmidt, A., Schrödner, R., Sorooshian, A., Stier, P., Toll, V., Watson-Parris, D., Wood, R., Yang, M., and Yuan, T.: Opportunistic experiments to constrain aerosol effective radiative forcing, Atmos. Chem. Phys., 22, 641–674, https://doi.org/10.5194/acp-22-641-2022, 2022.

Craig, P. S., Goldstein, M., Seheult, A. H., and Smith, J. A.: Pressure Matching for Hydrocarbon Reservoirs: A Case Study in the Use of Bayes Linear Strategies for Large Computer Experiments, in: Case Studies in Bayesian Statistics, vol. 121, edited
755 by: Gatsonis, C., Hodges, J. S., Kass, R. E., McCulloch, R., Rossi, P., and Singpurwalla, N. D., Springer New York, New York, NY, 37–93, https://doi.org/10.1007/978-1-4612-2290-3_2, 1997a.

Craig, P. S., Goldstein, M., Seheult, A. H., and Smith, J. A.: Pressure Matching for Hydrocarbon Reservoirs: A Case Study in the Use of Bayes Linear Strategies for Large Computer Experiments, in: Case Studies in Bayesian Statistics, vol. 121, edited by: Gatsonis, C., Hodges, J. S., Kass, R. E., McCulloch, R., Rossi, P., and Singpurwalla, N. D., Springer New York, New 760 York, NY, 37–93, https://doi.org/10.1007/978-1-4612-2290-3_2, 1997b.

Elsaesser, G. S., O'Dell, C. W., Lebsock, M. D., Bennartz, R., Greenwald, T. J., and Wentz, F. J.: The Multisensor Advanced Climatology of Liquid Water Path (MAC-LWP), J. Climate, 30, 10193–10210, https://doi.org/10.1175/JCLI-D-16-0902.1, 2017.

Eyring, V., Bony, S., Meehl, G. A., Senior, C. A., Stevens, B., Stouffer, R. J., and Taylor, K. E.: Overview of the Coupled 765 Model Intercomparison Project Phase 6 (CMIP6) experimental design and organization, Geosci. Model Dev., 9, 1937–1958, https://doi.org/10.5194/gmd-9-1937-2016, 2016.

Forster, P., Storelvmo, T., Armour, K., Collins, W., Dufresne, J., Frame, D., Lunt, D., Mauritsen, T., Palmer, M., Watanabe, M., Wild, M., and Zhang, H.: The Earth's energy budget, climate feedbacks, and climate sensitivity, in: Climate Change 2021: The Physical Science Basis. Contribution of Working Group I to the Sixth Assessment Report of the Intergovernmental Panel 770 on Climate Change, V. Masson-Delmotte, P. Zhai, A. Pirani, S. L. Connors, C. Pean, S. Berger, N. Caud, Y. Chen, L. Goldfarb, M. I. Gomis, M. Huang, K. Leitzell, E. Lonnoy, J. B. R. Matthews, T. K. Maycock, T. Aterfield, O. Yelekci, R. Yu and B. Zhou, Cambridge University Press, 2021.

Fyfe, J. C., Kharin, V. V., Santer, B. D., Cole, J. N. S., and Gillett, N. P.: Significant impact of forcing uncertainty in a large ensemble of climate model simulations, Proc. Natl. Acad. Sci. U.S.A., 118, e2016549118, 775 https://doi.org/10.1073/pnas.2016549118, 2021.

GCPC: https://psl.noaa.gov/data/gridded/data.gpcp.html.

CAMS global biomass burning emissions based on fire radiative power (GFAS): data documentation: https://confluence.ecmwf.int/display/CKB/CAMS+global+biomass+burning+emissions+based+on+fire+radiative+power+%28GFAS%29%3A+data+documentation.

780 Ghan, S., Wang, M., Zhang, S., Ferrachat, S., Gettelman, A., Griesfeller, J., Kipling, Z., Lohmann, U., Morrison, H., Neubauer, D., Partridge, D. G., Stier, P., Takemura, T., Wang, H., and Zhang, K.: Challenges in constraining anthropogenic aerosol effects on cloud radiative forcing using present-day spatiotemporal variability, Proc Natl Acad Sci USA, 113, 5804–5811, https://doi.org/10.1073/pnas.1514036113, 2016.

Gliß, J., Mortier, A., Schulz, M., Andrews, E., Balkanski, Y., Bauer, S. E., Benedictow, A. M. K., Bian, H., Checa-Garcia, R., 785 Chin, M., Ginoux, P., Griesfeller, J. J., Heckel, A., Kipling, Z., Kirkevåg, A., Kokkola, H., Laj, P., Le Sager, P., Lund, M. T., Lund Myhre, C., Matsui, H., Myhre, G., Neubauer, D., van Noije, T., North, P., Olivié, D. J. L., Rémy, S., Sogacheva, L., Takemura, T., Tsigaridis, K., and Tsyro, S. G.: AeroCom phase III multi-model evaluation of the aerosol life cycle and optical properties using ground- and space-based remote sensing as well as surface in situ observations, Atmos. Chem. Phys., 21, 87–128, https://doi.org/10.5194/acp-21-87-2021, 2021.

790 Gordon, H., Field, P. R., Abel, S. J., Dalvi, M., Grosvenor, D. P., Hill, A. A., Johnson, B. T., Miltenberger, A. K., Yoshioka, M., and Carslaw, K. S.: Large simulated radiative effects of smoke in the south-east Atlantic, Atmos. Chem. Phys., 18, 15261–15289, https://doi.org/10.5194/acp-18-15261-2018, 2018.

Grosvenor, D. P. and Carslaw, K. S.: The decomposition of cloud–aerosol forcing in the UK Earth System Model (UKESM1), Atmos. Chem. Phys., 20, 15681–15724, https://doi.org/10.5194/acp-20-15681-2020, 2020.

795 Grosvenor, D. P., Field, P. R., Hill, A. A., and Shipway, B. J.: The relative importance of macrophysical and cloud albedo changes for aerosol-induced radiative effects in closed-cell stratocumulus: insight from the modelling of a case study, Atmos. Chem. Phys., 17, 5155–5183, https://doi.org/10.5194/acp-17-5155-2017, 2017.

Gryspeerdt, E., Quaas, J., and Bellouin, N.: Constraining the aerosol influence on cloud fraction: AEROSOLS AND CLOUD FRACTION, J. Geophys. Res. Atmos., 121, 3566–3583, https://doi.org/10.1002/2015JD023744, 2016.

800 Halmer, M. M., Schmincke, H.-U., and Graf, H.-F.: The annual volcanic gas input into the atmosphere, in particular into the stratosphere: a global data set for the past 100 years, Journal of Volcanology and Geothermal Research, 115, 511–528, https://doi.org/10.1016/S0377-0273(01)00318-3, 2002.

Hamilton, D. S., Lee, L. A., Pringle, K. J., Reddington, C. L., Spracklen, D. V., and Carslaw, K. S.: Occurrence of pristine aerosol environments on a polluted planet, Proc Natl Acad Sci USA, 111, 18466–18471,
805 https://doi.org/10.1073/pnas.1415440111, 2014.

Hill, A. A., Shipway, B. J., and Boutle, I. A.: How sensitive are aerosol-precipitation interactions to the warm rain representation?: RESPONSE OF ACI TO WARM RAIN SCHEME, J. Adv. Model. Earth Syst., 7, 987–1004, https://doi.org/10.1002/2014MS000422, 2015.

Hourdin, F., Mauritsen, T., Gettelman, A., Golaz, J.-C., Balaji, V., Duan, Q., Folini, D., Ji, D., Klocke, D., Qian, Y., Rauser,
810 F., Rio, C., Tomassini, L., Watanabe, M., and Williamson, D.: The Art and Science of Climate Model Tuning, Bulletin of the American Meteorological Society, 98, 589–602, https://doi.org/10.1175/BAMS-D-15-00135.1, 2017.

Johnson, J. S., Regayre, L. A., Yoshioka, M., Pringle, K. J., Turnock, S. T., Browse, J., Sexton, D. M. H., Rostron, J. W., Schutgens, N. A. J., Partridge, D. G., Liu, D., Allan, J. D., Coe, H., Ding, A., Cohen, D. D., Atanacio, A., Vakkari, V., Asmi, E., and Carslaw, K. S.: Robust observational constraint of uncertain aerosol processes and emissions in a climate model and
815 the effect on aerosol radiative forcing, Atmos. Chem. Phys., 20, 9491–9524, https://doi.org/10.5194/acp-20-9491-2020, 2020.

Kim, S.: pcor: An R Package for a Fast Calculation to Semi-partial Correlation Coefficients, Communications for Statistical Applications and Methods, 22, 665–674, 2015.

King, M. D., Menzel, W. P., Kaufman, Y. J., Tanre, D., Bo-Cai Gao, Platnick, S., Ackerman, S. A., Remer, L. A., Pincus, R., and Hubanks, P. A.: Cloud and aerosol properties, precipitable water, and profiles of temperature and water vapor from
820 MODIS, IEEE Trans. Geosci. Remote Sensing, 41, 442–458, https://doi.org/10.1109/TGRS.2002.808226, 2003.

Langton, T., Stier, P., Watson-Parris, D., and Mulcahy, J. P.: Decomposing Effective Radiative Forcing Due to Aerosol Cloud Interactions by Global Cloud Regimes, Geophys Res Lett, 48, https://doi.org/10.1029/2021GL093833, 2021.

Lebsock, M., Morrison, H., and Gettelman, A.: Microphysical implications of cloud-precipitation covariance derived from satellite remote sensing: CLOUD-PRECIPITATION COVARIANCE, J. Geophys. Res. Atmos., 118, 6521–6533,
825 https://doi.org/10.1002/jgrd.50347, 2013.

Lee, L. A., Carslaw, K. S., Pringle, K. J., and Mann, G. W.: Mapping the uncertainty in global CCN using emulation, Atmos. Chem. Phys., 12, 9739–9751, https://doi.org/10.5194/acp-12-9739-2012, 2012.

Lee, L. A., Reddington, C. L., and Carslaw, K. S.: On the relationship between aerosol model uncertainty and radiative forcing uncertainty, Proc Natl Acad Sci USA, 113, 5820–5827, https://doi.org/10.1073/pnas.1507050113, 2016.

830   Mann, G. W., Carslaw, K. S., Spracklen, D. V., Ridley, D. A., Manktelow, P. T., Chipperfield, M. P., Pickering, S. J., and Johnson, C. E.: Description and evaluation of GLOMAP-mode: a modal global aerosol microphysics model for the UKCA composition-climate model, Geosci. Model Dev., 3, 519–551, https://doi.org/10.5194/gmd-3-519-2010, 2010.

Mann, G. W., Carslaw, K. S., Ridley, D. A., Spracklen, D. V., Pringle, K. J., Merikanto, J., Korhonen, H., Schwarz, J. P., Lee, L. A., Manktelow, P. T., Woodhouse, M. T., Schmidt, A., Breider, T. J., Emmerson, K. M., Reddington, C. L., Chipperfield, 835   M. P., and Pickering, S. J.: Intercomparison of modal and sectional aerosol microphysics representations within the same 3-D global chemical transport model, Atmos. Chem. Phys., 12, 4449–4476, https://doi.org/10.5194/acp-12-4449-2012, 2012.

McComiskey, A., Feingold, G., Frisch, A. S., Turner, D. D., Miller, M. A., Chiu, J. C., Min, Q., and Ogren, J. A.: An assessment of aerosol-cloud interactions in marine stratus clouds based on surface remote sensing, J. Geophys. Res., 114, D09203, https://doi.org/10.1029/2008JD011006, 2009.

840   McCoy, I. L., McCoy, D. T., Wood, R., Regayre, L., Watson-Parris, D., Grosvenor, D. P., Mulcahy, J. P., Hu, Y., Bender, F. A.-M., Field, P. R., Carslaw, K. S., and Gordon, H.: The hemispheric contrast in cloud microphysical properties constrains aerosol forcing, Proceedings of the National Academy of Sciences, 117, 189980–19006, https://doi.org/10.1073/pnas.1922502117, 2020.

McNeall, D., Williams, J., Booth, B., Betts, R., Challenor, P., Wiltshire, A., and Sexton, D.: The impact of structural error on 845   parameter constraint in a climate model, Earth Syst. Dynam., 7, 917–935, https://doi.org/10.5194/esd-7-917-2016, 2016.

Metzger, A., Verheggen, B., Dommen, J., Duplissy, J., Prevot, A. S. H., Weingartner, E., Riipinen, I., Kulmala, M., Spracklen, D. V., Carslaw, K. S., and Baltensperger, U.: Evidence for the role of organics in aerosol particle formation under atmospheric conditions, Proc. Natl. Acad. Sci. U.S.A., 107, 6646–6651, https://doi.org/10.1073/pnas.0911330107, 2010.

MODIS: https://modis.gsfc.nasa.gov/data/dataprod/mod06.php.

850   Mulcahy, J. P., Jones, C., Sellar, A., Johnson, B., Boutle, I. A., Jones, A., Andrews, T., Rumbold, S. T., Mollard, J., Bellouin, N., Johnson, C. E., Williams, K. D., Grosvenor, D. P., and McCoy, D. T.: Improved Aerosol Processes and Effective Radiative Forcing in HadGEM3 and UKESM1, J. Adv. Model. Earth Syst., 10, 2786–2805, https://doi.org/10.1029/2018MS001464, 2018.

Mulcahy, J. P., Johnson, C., Jones, C. G., Povey, A. C., Scott, C. E., Sellar, A., Turnock, S. T., Woodhouse, M. T., Abraham, 855   N. L., Andrews, M. B., Bellouin, N., Browse, J., Carslaw, K. S., Dalvi, M., Folberth, G. A., Glover, M., Grosvenor, D. P., Hardacre, C., Hill, R., Johnson, B., Jones, A., Kipling, Z., Mann, G., Mollard, J., O'Connor, F. M., Palmiéri, J., Reddington, C., Rumbold, S. T., Richardson, M., Schutgens, N. A. J., Stier, P., Stringer, M., Tang, Y., Walton, J., Woodward, S., and Yool, A.: Description and evaluation of aerosol in UKESM1 and HadGEM3-GC3.1 CMIP6 historical simulations, Geosci. Model Dev., 13, 6383–6423, https://doi.org/10.5194/gmd-13-6383-2020, 2020.

860   O'Hagan, A.: Bayesian analysis of computer code outputs: A tutorial, Reliability Engineering & System Safety, 91, 1290–1300, https://doi.org/10.1016/j.ress.2005.11.025, 2006.

Painemal, D. and Zuidema, P.: Assessment of MODIS cloud effective radius and optical thickness retrievals over the Southeast Pacific with VOCALS-REx in situ measurements: MODIS VALIDATION DURING VOCALS-REx, J. Geophys. Res., 116, n/a-n/a, https://doi.org/10.1029/2011JD016155, 2011.

865   Peace, A. H., Carslaw, K. S., Lee, L. A., Regayre, L. A., Booth, B. B. B., Johnson, J. S., and Bernie, D.: Effect of aerosol radiative forcing uncertainty on projected exceedance year of a 1.5 °C global temperature rise, Environ. Res. Lett., 15, 0940a6, https://doi.org/10.1088/1748-9326/aba20c, 2020.

Qian, Y., Wan, H., Yang, B., Golaz, J., Harrop, B., Hou, Z., Larson, V. E., Leung, L. R., Lin, G., Lin, W., Ma, P., Ma, H., Rasch, P., Singh, B., Wang, H., Xie, S., and Zhang, K.: Parametric Sensitivity and Uncertainty Quantification in the Version 1 of E3SM Atmosphere Model Based on Short Perturbed Parameter Ensemble Simulations, J. Geophys. Res. Atmos., 123, https://doi.org/10.1029/2018JD028927, 2018.

Regayre, L. A., Pringle, K. J., Lee, L. A., Rap, A., Browse, J., Mann, G. W., Reddington, C. L., Carslaw, K. S., Booth, B. B. B., and Woodhouse, M. T.: The Climatic Importance of Uncertainties in Regional Aerosol–Cloud Radiative Forcings over Recent Decades, Journal of Climate, 28, 6589–6607, https://doi.org/10.1175/JCLI-D-15-0127.1, 2015.

Regayre, L. A., Johnson, J. S., Yoshioka, M., Pringle, K. J., Sexton, D. M. H., Booth, B. B. B., Lee, L. A., Bellouin, N., and Carslaw, K. S.: Aerosol and physical atmosphere model parameters are both important sources of uncertainty in aerosol ERF, Atmos. Chem. Phys., 18, 9975–10006, https://doi.org/10.5194/acp-18-9975-2018, 2018.

Regayre, L. A., Schmale, J., Johnson, J. S., Tatzelt, C., Baccarini, A., Henning, S., Yoshioka, M., Stratmann, F., Gysel-Beer, M., Grosvenor, D. P., and Carslaw, K. S.: The value of remote marine aerosol measurements for constraining radiative forcing uncertainty, Atmos. Chem. Phys., 20, 10063–10072, https://doi.org/10.5194/acp-20-10063-2020, 2020.

Regayre, L. A., Carslaw, K. S., Deaconu, L., Symonds, C., Richardson, M., Langton, T., Watson-Parris, D., and Stier, P.: A-CURE: Monthly mean perturbed parameter ensemble data, https://catalogue.ceda.ac.uk/uuid/b735718d66c1403fbf6b93ba3bd3b1a9.

Rostron, J. W., Sexton, D. M. H., McSweeney, C. F., Yamazaki, K., Andrews, T., Furtado, K., Ringer, M. A., and Tsushima, Y.: The impact of performance filtering on climate feedbacks in a perturbed parameter ensemble, Clim Dyn, 55, 521–551, https://doi.org/10.1007/s00382-020-05281-8, 2020.

Saponaro, G., Sporre, M. K., Neubauer, D., Kokkola, H., Kolmonen, P., Sogacheva, L., Arola, A., de Leeuw, G., Karset, I. H. H., Laaksonen, A., and Lohmann, U.: Evaluation of aerosol and cloud properties in three climate models using MODIS observations and its corresponding COSP simulator, as well as their application in aerosol–cloud interactions, Atmos. Chem. Phys., 20, 1607–1626, https://doi.org/10.5194/acp-20-1607-2020, 2020.

Schmale, J., Baccarini, A., Thurnherr, I., Henning, S., Efraim, A., Regayre, L., Bolas, C., Hartmann, M., Welti, A., Lehtipalo, K., Aemisegger, F., Tatzelt, C., Landwehr, S., Modini, R. L., Tummon, F., Johnson, J. S., Harris, N., Schnaiter, M., Toffoli, A., Derkani, M., Bukowiecki, N., Stratmann, F., Dommen, J., Baltensperger, U., Wernli, H., Rosenfeld, D., Gysel-Beer, M., and Carslaw, K. S.: Overview of the Antarctic Circumnavigation Expedition: Study of Preindustrial-like Aerosols and Their Climate Effects (ACE-SPACE), Bulletin of the American Meteorological Society, 100, 2260–2283, https://doi.org/10.1175/BAMS-D-18-0187.1, 2019.

Schutgens, N., Tsyro, S., Gryspeerdt, E., Goto, D., Weigum, N., Schulz, M., and Stier, P.: On the spatio-temporal representativeness of observations, Atmos. Chem. Phys., 17, 9761–9780, https://doi.org/10.5194/acp-17-9761-2017, 2017.

Seinfeld, J. H., Bretherton, C., Carslaw, K. S., Coe, H., DeMott, P. J., Dunlea, E. J., Feingold, G., Ghan, S., Guenther, A. B., Kahn, R., Kraucunas, I., Kreidenweis, S. M., Molina, M. J., Nenes, A., Penner, J. E., Prather, K. A., Ramanathan, V., Ramaswamy, V., Rasch, P. J., Ravishankara, A. R., Rosenfeld, D., Stephens, G., and Wood, R.: Improving our fundamental understanding of the role of aerosol−cloud interactions in the climate system, Proc. Natl. Acad. Sci. U.S.A., 113, 5781–5790, https://doi.org/10.1073/pnas.1514043113, 2016.

Sellar, A. A., Jones, C. G., Mulcahy, J. P., Tang, Y., Yool, A., Wiltshire, A., O'Connor, F. M., Stringer, M., Hill, R., Palmieri, J., Woodward, S., Mora, L., Kuhlbrodt, T., Rumbold, S. T., Kelley, D. I., Ellis, R., Johnson, C. E., Walton, J., Abraham, N. L., Andrews, M. B., Andrews, T., Archibald, A. T., Berthou, S., Burke, E., Blockley, E., Carslaw, K., Dalvi, M., Edwards, J., Folberth, G. A., Gedney, N., Griffiths, P. T., Harper, A. B., Hendry, M. A., Hewitt, A. J., Johnson, B., Jones, A., Jones, C. D.,

Keeble, J., Liddicoat, S., Morgenstern, O., Parker, R. J., Predoi, V., Robertson, E., Siahaan, A., Smith, R. S., Swaminathan, R., Woodhouse, M. T., Zeng, G., and Zerroukat, M.: UKESM1: Description and Evaluation of the U.K. Earth System Model, 910 J. Adv. Model. Earth Syst., 11, 4513–4558, https://doi.org/10.1029/2019MS001739, 2019.

Sengupta, K., Pringle, K., Johnson, J. S., Reddington, C., Browse, J., Scott, C. E., and Carslaw, K.: A global model perturbed parameter ensemble study of secondary organic aerosol formation, Atmos. Chem. Phys., 21, 2693–2723, https://doi.org/10.5194/acp-21-2693-2021, 2021.

Sexton, D. M. H., Murphy, J. M., Collins, M., and Webb, M. J.: Multivariate probabilistic projections using imperfect climate 915 models part I: outline of methodology, Clim Dyn, 38, 2513–2542, https://doi.org/10.1007/s00382-011-1208-9, 2012.

Sexton, D. M. H., McSweeney, C. F., Rostron, J. W., Yamazaki, K., Booth, B. B. B., Murphy, J. M., Regayre, L., Johnson, J. S., and Karmalkar, A. V.: A perturbed parameter ensemble of HadGEM3-GC3.05 coupled model projections: part 1: selecting the parameter combinations, Clim Dyn, 56, 3395–3436, https://doi.org/10.1007/s00382-021-05709-9, 2021.

Shipway, B. J. and Hill, A. A.: Diagnosis of systematic differences between multiple parametrizations of warm rain 920 microphysics using a kinematic framework, Q.J.R. Meteorol. Soc., 138, 2196–2211, https://doi.org/10.1002/qj.1913, 2012.

Skeie, R. B., Berntsen, T., Aldrin, M., Holden, M., and Myhre, G.: A lower and more constrained estimate of climate sensitivity using updated observations and detailed radiative forcing time series, Earth Syst. Dynam., 5, 139–175, https://doi.org/10.5194/esd-5-139-2014, 2014.

Skeie, R. B., Berntsen, T., Aldrin, M., Holden, M., and Myhre, G.: Climate sensitivity estimates – sensitivity to radiative 925 forcing time series and observational data, Earth Syst. Dynam., 9, 879–894, https://doi.org/10.5194/esd-9-879-2018, 2018.

Smith, C. J., Harris, G. R., Palmer, M. D., Bellouin, N., Collins, W., Myhre, G., Schulz, M., Golaz, J. -C., Ringer, M., Storelvmo, T., and Forster, P. M.: Energy Budget Constraints on the Time History of Aerosol Forcing and Climate Sensitivity, Geophys Res Atmos, 126, https://doi.org/10.1029/2020JD033622, 2021.

Stocki, R.: A method to improve design reliability using optimal Latin hypercube sampling, Comp. Ass. Mech. Eng. Sci., 12, 930 87–105, 2005.

Thornhill, G., Collins, W., Olivié, D., Skeie, R. B., Archibald, A., Bauer, S., Checa-Garcia, R., Fiedler, S., Folberth, G., Gjermundsen, A., Horowitz, L., Lamarque, J.-F., Michou, M., Mulcahy, J., Nabat, P., Naik, V., O'Connor, F. M., Paulot, F., Schulz, M., Scott, C. E., Séférian, R., Smith, C., Takemura, T., Tilmes, S., Tsigaridis, K., and Weber, J.: Climate-driven chemistry and aerosol feedbacks in CMIP6 Earth system models, Atmos. Chem. Phys., 21, 1105–1126, 935 https://doi.org/10.5194/acp-21-1105-2021, 2021.

Vernon, I., Goldstein, M., and Bower, R.: Galaxy Formation: Bayesian History Matching for the Observable Universe, Statist. Sci., 29, https://doi.org/10.1214/12-STS412, 2014.

Vignesh, P., Jiang, J., Kishore, P., Su, H., Smay, T., Brighton, N., and Velicogna, I.: Assessment of CMIP6 Cloud Fraction and Comparison with Satellite Observations, Earth and Space Science, 7, https://doi.org/10.1029/2019EA00097, 2020.

940 Walters, D., Baran, A. J., Boutle, I., Brooks, M., Earnshaw, P., Edwards, J., Furtado, K., Hill, P., Lock, A., Manners, J., Morcrette, C., Mulcahy, J., Sanchez, C., Smith, C., Stratton, R., Tennant, W., Tomassini, L., Van Weverberg, K., Vosper, S., Willett, M., Browse, J., Bushell, A., Carslaw, K., Dalvi, M., Essery, R., Gedney, N., Hardiman, S., Johnson, B., Johnson, C., Jones, A., Jones, C., Mann, G., Milton, S., Rumbold, H., Sellar, A., Ujiie, M., Whitall, M., Williams, K., and Zerroukat, M.: The Met Office Unified Model Global Atmosphere 7.0/7.1 and JULES Global Land 7.0 configurations, Geosci. Model Dev., 945 12, 1909–1963, https://doi.org/10.5194/gmd-12-1909-2019, 2019.

Watson-Parris, D., Bellouin, N., Deaconu, L. T., Schutgens, N. A. J., Yoshioka, M., Regayre, L. A., Pringle, K. J., Johnson, J. S., Smith, C. J., Carslaw, K. S., and Stier, P.: Constraining Uncertainty in Aerosol Direct Forcing, Geophys. Res. Lett., 47, https://doi.org/10.1029/2020GL087141, 2020.

Watson-Parris, D., Williams, A., Deaconu, L., and Stier, P.: Model calibration using ESEm v1.1.0 – an open, scalable Earth
950 system emulator, Geosci. Model Dev., 14, 7659–7672, https://doi.org/10.5194/gmd-14-7659-2021, 2021.

West, R. E. L., Stier, P., Jones, A., Johnson, C. E., Mann, G. W., Bellouin, N., Partridge, D. G., and Kipling, Z.: The importance of vertical velocity variability for estimates of the indirect aerosol effects, Atmos. Chem. Phys., 14, 6369–6393, https://doi.org/10.5194/acp-14-6369-2014, 2014.

Williams, A. I. L., Stier, P., Dagan, G., and Watson-Parris, D.: Strong control of effective radiative forcing by the spatial
955 pattern of absorbing aerosol, Nat. Clim. Chang., 12, 735–742, https://doi.org/10.1038/s41558-022-01415-4, 2022.

Williams, K. D., Copsey, D., Blockley, E. W., Bodas-Salcedo, A., Calvert, D., Comer, R., Davis, P., Graham, T., Hewitt, H. T., Hill, R., Hyder, P., Ineson, S., Johns, T. C., Keen, A. B., Lee, R. W., Megann, A., Milton, S. F., Rae, J. G. L., Roberts, M. J., Scaife, A. A., Schiemann, R., Storkey, D., Thorpe, L., Watterson, I. G., Walters, D. N., West, A., Wood, R. A., Woollings, T., and Xavier, P. K.: The Met Office Global Coupled Model 3.0 and 3.1 (GC3.0 and GC3.1) Configurations, J. Adv. Model.
960 Earth Syst., 10, 357–380, https://doi.org/10.1002/2017MS001115, 2018.

Williamson, D., Goldstein, M., Allison, L., Blaker, A., Challenor, P., Jackson, L., and Yamazaki, K.: History matching for exploring and reducing climate model parameter space using observations and a large perturbed physics ensemble, Clim Dyn, 41, 1703–1729, https://doi.org/10.1007/s00382-013-1896-4, 2013.

Woodward, S.: Modeling the atmospheric life cycle and radiative impact of mineral dust in the Hadley Centre climate model,
965 J. Geophys. Res., 106, 18155–18166, https://doi.org/10.1029/2000JD900795, 2001.

Yoshioka, M., Regayre, L. A., Pringle, K. J., Johnson, J. S., Mann, G. W., Partridge, D. G., Sexton, D. M. H., Lister, G. M. S., Schutgens, N., Stier, P., Kipling, Z., Bellouin, N., Browse, J., Booth, B. B. B., Johnson, C. E., Johnson, B., Mollard, J. D. P., Lee, L., and Carslaw, K. S.: Ensembles of Global Climate Model Variants Designed for the Quantification and Constraint of Uncertainty in Aerosols and Their Radiative Forcing, J. Adv. Model. Earth Syst., 11, 3728–3754,
970 https://doi.org/10.1029/2019MS001628, 2019.